SHARED CONTROL IN AERIAL CYBER-PHYSICAL HUMAN SYSTEMS

A THESIS SUBMITTED TO

THE GRADUATE SCHOOL OF ENGINEERING AND SCIENCE

OF BILKENT UNIVERSITY

IN PARTIAL FULFILLMENT OF THE REQUIREMENTS FOR

THE DEGREE OF

MASTER OF SCIENCE

IN

MECHANICAL ENGINEERING

By

Emre Eraslan

June 2021

Shared Control in Aerial Cyber-Physical Human Systems
By Emre Eraslan
June 2021

We certify that we have read this thesis and that in our opinion it is fully adequate, in scope and in quality, as a thesis for the degree of Master of Science.

Yıldıray Yıldız(Advisor)

Onur Özcan

Mustafa Mert Ankaralı

Approved for the Graduate School of Engineering and Science:

Ezhan Karaşan
Director of the Graduate School

ABSTRACT

SHARED CONTROL IN AERIAL CYBER-PHYSICAL HUMAN SYSTEMS

Emre Eraslan
M.S. in Mechanical Engineering
Advisor: Yıldıray Yıldız
June 2021

This study considers the problem of control when two distinct decision makers, a human operator and an advanced automation working together, face severe uncertainties and anomalies. Under the rubric of Cyber-Physical Human Systems, we focus on shared control architectures (SCAs) that allow an advantageous combination of human/automation abilities and provide a desired resilient performance. Humans and automation are likely to be interchangeable for routine tasks under normal conditions. However, under severe anomalies, the two entities provide complementary actions. It could be argued that human experts excel at cognitive tasks, such as anomaly recognition and estimation, while fast response with reduced latencies may be better accomplished by automation. For severe anomalies, we propose the use of a common metric called *capacity for maneuver* (CfM) that enables a smooth, bumpless transition when severe anomalies occur. It can be identified in control systems as the actuator's proximity to its limits of saturation. Three different SCAs are presented, two of which use CfM by describing how human experts and automation can participate in a shared control action and recover gracefully from anomalous situations. Two of the SCAs are validated using human-in-the-loop experiments. The last SCA is exemplified theoretically, in which an analytical framework for the equations of motion of flexible quadrotor unmanned aerial vehicles is derived. A low-frequency adaptive controller together with a human pilot model is implemented using the developed model to prevent excessive oscillations due to flexible dynamics and to compensate uncertainties.

Keywords: cyber-physical human systems, shared control architecture, capacity for maneuver, closed loop reference model adaptive control, flexible quadrotor UAV.

ÖZET

HAVASAL SİBER-FİZİKSEL İNSAN SİSTEMLERİNDE PAYLAŞIMLI KONTROL

Emre Eraslan
Makina Mühendisliği, Yüksek Lisans
Tez Danışmanı: Yıldıray Yıldız
Haziran 2021

Bu çalışma bir insan operatör ve ileri düzey otomasyon birlikte çalışırken belirsizlikler ve anomalilerle karşı karşıya kaldıklarında meydana gelen kontrol sorununu ele almaktadır. Siber-Fiziksel İnsan Sistemleri başlığı altında, insan ve otomasyon yeteneklerinin avantajlı bir kombinasyonuna izin veren ve istenen performansı sağlayan paylaşımlı kontrol mimarilerine (PKM) odaklanmaktayız. İnsan ve otomasyon normal koşullar altında rutin görevler için birbirlerinin yerine geçebilir. Ancak, ciddi anomaliler altında kendilerine özgü tepkiler verebilirler. İnsanlar anomali tanıma ve tahmin etme gibi bilişsel görevlerde başarılıyken, otomasyon gecikme sürelerinin az olduğu hızlı yanıtlar verebilir. Biz bu tezde şiddetli anomalilerin olduğu durumlarda insan ve otomasyon arasındaki kontrol geçişlerinin sorunsuz bir şekilde gerçekleşmesini sağlayacak *manevra kapasitesi* (MK) adlı bir metrik kullanılmasını öneriyoruz. Bu metrik, kontrol sistemlerinde eyleyicilerin doyma sınırlarına yakınlığı olarak tanımlanabilir. Bu tezde sunulan üç farklı PKM'nin ikisinde MK'den faydalanılmış, insanın ve otomasyonun paylaşımlı kontrole nasıl katkı yaptıkları ve anomali durumlardan nasıl kaçınıldığı tasvir edilmiştir. Bu PKM'lerden ikisi döngüde-insan deneyleri kullanılarak doğrulanmıştır. Son PKM'de ise, esnek bir dört pervaneli insansız hava aracının hareket denklemleri çıkarılmış ve tüm sistem simülasyonlar ile doğrulanmıştır. Bu son yaklaşımda, insan modeliyle birlikte esnek dinamiklerden kaynaklanan titreşimleri azaltmak ve belirsizlikleri telafi etmek için düşük frekanslı uyarlamalı bir kontrolcü kullanılmıştır.

Anahtar sözcükler: siber-fiziksel insan sistemleri, paylaşımlı kontrol mimarisi, manevra kapasitesi, kapalı döngü referans modelli uyarlamalı kontrol, elastik dört pervaneli İHA.

Acknowledgement

I would like to express the deepest appreciation to my thesis supervisor *Dr. Yıldıray Yıldız* who provided invaluable feedback on my studies, experiments and methods by responding to emails literally anytime in the whole day and even staying up late in the office with full of discussions about paper revisions. It has been a privilege working in his lab 'Systems Laboratory' and contributing to top-notch research. I never would have been able to finish this work without his unfailing support and continuous encouragement.

I am indebted also to the PhD candidate *Shahabaldin Tohidi*, the dear member of the Systems Laboratory, for letting me make use of his deep knowledge of control systems and helping me with my questions whenever and wherever I am stuck.

Very special thanks to *Didem Demir, Berkay Şahinoğlu, Atakan Atay* and *Büşra Sarıarslan*! Without you, the graduate office would have been very silent and unbearable. Thank you for your camaraderie and support. Your friendship have rendered my life more enjoyable and will always be remembered. I am also extremely thankful to the other members of the graduate office who have sincerely contributed to my human-in-the-loop experiments.

Lastly, my family deserves endless gratitude: my father for his unfailing support and faith, and my mother for her unconditional love who helped me experimentally verify the saying 'Behind every successful man is a woman', and finally my cat for her existence that gives me the utmost peace.

It should be noted that this research was supported partially under the grant of 118E202 (chapters 1, 2 and 4) and partially under the grant of 118E937 (chapters 1, 3 and 4) funded by The Scientific and Technological Research Council of Turkey (TÜBİTAK).

Contents

List of Figures

List of Tables

Chapter 1

Introduction

1.1 Cyber-Physical Human Systems

The 21st century has been witnessing enormous transformations in several sectors including energy, water, transportation, robotics, manufacturing, and health care relevant to autonomy. Taking these developments into consideration, it is frequently observed that the autonomous systems alone no longer prove sufficient in some uncertain and anomalous applications which generally require the presence and supervision of higher decision-making mechanisms, in other words, the humans themselves [1]. In the light of this fact, it can be inferred that the collaboration of humans and automation could be a promising solution to the control problem of such applications.

A system in which human operators, plants, and other cyber and physical components interact to achieve a goal is called cyberphysical human system (CPHS). In a CPHS, humans are considered indispensable, contributing to communication, control and especially cognitive features that an automated system may lack. In this aspect, the collaboration of autonomous systems and humans demonstrate a goal-oriented behavior in understanding the task and responding to changing goals flexibly [2]. It is therefore expected that CPHSs operate better in unpredictable environments and adapt themselves faster to dynamic changes. A specific type of CPHS, namely "shared control architectures" (SCA) is the focus of this thesis.

1.2 Shared Control Architectures (SCAs)

An autonomous system is expected to make decisions and take actions using real-time information and to adapt online in the presence of uncertainties and anomalies. Uncertainties may occur in both structured and unstructured forms. Anomalies may often be severe that require rapid detection and rapid action [1]. In the specific context of flight control systems, pilots regularly make decisions under anomalous situations whereas autopilots follow the given commands.

When an anomaly is detected, the pilot and autopilot may act differently to alleviate the severity of this anomaly. It may be contended that the detection of the anomaly can be carried out more effectively by the pilot whilst a fast command tracking can be best achieved by an autopilot. Therefore a shared control architecture (SCA), where the decision making of the human pilot is combined with the capabilities of an advanced autopilot is a promising solution to many anomalous flight control problems.

Existing frameworks that consist of humans and automation are generally based on the premise that human experts back up the flight control automation: In this semi-autonomous system, the automation handles uncertainties and disturbances, and the human takes over control once the environment imposes demands that exceeds the capabilities of the automation [3, 4, 5]. This method may result in a bumpy and late transfer of control from the automation to the human, and hence the failure of the shared-control architecture, since it cannot keep pace with the increasing demand which may cause actual accidents [6, 7, 8, 9]. This then suggests that alternate architectures between the human expert and automation may be needed. These alternatives are introduced in the followings paragraphs.

The main distinction between the classification of SCAs is predicated on the timing of human and automation control inputs. In the literature, these architectures are grouped into three categories: a *traded* control action where humans take over control from automation under emergency conditions [10], a *supervised* control action where the pilot has a high-level role and provides inputs for the automation when necessary [11], and a *combined* control action where both the automation and the human pilot exert inputs at the same time scale [12].

In this thesis, all three forms of control architectures are collected under a collective name of *Shared Control Architecture* (SCA), with SCA1 as the trading action, SCA2 as the supervisory action, and SCA3 as the combined action (see Figure 1.1).

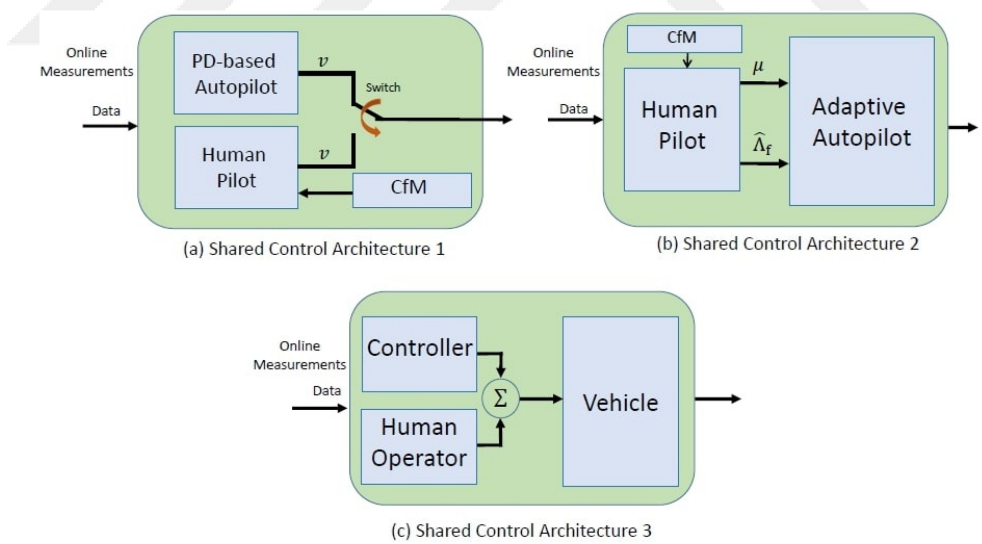

Figure 1.1: An overview of Shared Control Architectures (SCAs).

1.2.1 SCA1 as Traded Control

In SCA1, the authority shifts from the automation to the human pilot in case of emergency. For instance, in a teleoperation task, if a robot autonomously travels on the remote environment and at certain time-intervals a human operator takes over the control and provides real time speed and direction commands, then this type of interaction can be considered as traded control.

1.2.2 SCA2 as Supervisory Control

In SCA2, the human pilot is on-the-loop, and provides a supervisory, high-level input to the automation. One such example may occur again in the teleoperation scenario mentioned above, where the human operator can provide reference points for the mobile robot and the control system on the robot can autonomously navigate the vehicle, make it avoid obstacles and reach the reference points.

1.2.3 SCA3 as Combined Control

In SCA3, different from SCA1 and SCA2, the human and the automation are both active simultaneously. For example, in the discussed teleoperation task, if the human controls the robot via a joystick in real time and at the same time the robot controller continuously sends force inputs to the joystick to keep the robot collision-free on the terrain, then this can be considered as combined control.

In addition to the above, SCAs have been explored in haptic shared control (HSC), whose applications can be found in both aerospace [13] and automotive [12, 14] domains. In HSC, both operators apply force via a common control interface to accomplish a control goal. Therefore, this method of control architecture can be considered as SCA3. Another example can be found in [13] where the control goal of interest is to help a UAV operator avoid a collision with an obstacle via haptic feedback. In [14], SCA architecture is used for the lane-keeping task, and in [12], it is used for helping the driver while driving around a curve. It is observed that situational awareness of the human operator is improved in all of these approaches. In the specific area of flight control, examples of SCAs where the situational awareness of the pilots are improved can be found in [15, 16, 17, 18]. In these examples no severe anomalies are taken into consideration.

1.3 Contribution of This Thesis

The contributions of this thesis can be listed as follows:

- Effects of severe anomalies on SCAs are investigated experimentally.
- For SCA1, a specific switching mechanism based on the capacity for maneuver (CfM) is experimentally validated to provide a bumpless transfer of control while maintaining a high tracking performance.
- For SCA2, the notion of capacity for maneuver (CfM) is experimentally verified to perform a resilient flight control under severe anomalies.
- A controller robust to severe anomalies and uncertainties from user dynamics is put forward for the control problem of a foldable UAV.

1.4 Structure of the Thesis

The work done in this thesis can be compiled as follows. Chapter 2 introduces a new example of SCA1 as traded control and a new example of SCA2 as supervisory control. Both of these structures are validated using human-in-the-loop experiments. This chapter is mainly based on [1]. Chapter 3 elaborates on the derivation of the equations of motion of a flexible quadrotor UAV starting from the first principles and includes a human-in-the-loop stability analysis as a reference to a different kind of SCA. This chapter is based on [19]. Finally, Chapter 4 summarizes the work and discusses future work.

Chapter 2

Shared Control Between Pilots and Autopilots: SCA1 & SCA2

In this chapter, new SCA1 and SCA2 examples are introduced with the help of two principles from cognitive engineering that are developed to help add resilience to complex systems [6, 7, 9]. The first principle is Capacity for Maneuver (CfM), which denotes the reserve capacity of a system that remains after the occurrence of an anomaly [7]. It is suggested that resiliency can be accomplished via monitoring and regulation of the CfM [9]. The notion of CfM exists in an engineering context as well, which is the reserved capacity of an actuator. Viewing the actuator input power as the system's capacity, and noting that a fundamental capacity limit exists in all actuators in the form of magnitude saturation, one can define CfM for an autopilot-controlled system as the distance between the control input and saturation limits. The need to avoid actuator saturation, and therefore increasing CfM, becomes even more urgent in the face of anomalies which may push the actuators to their limits. This implies that there is a common link between a pilot-based decision making with that of an autopilot-based one in the form of CfM.

The foundations for SCA1 and SCA2 investigated in this chapter come from the results of [20, 21, 22], with [20] and [21] corresponding to SCA1 and [22] corresponding to SCA2. In [20], the assumption is that the autopilot is designed to accommodate satisfactory operation under nominal conditions, with the requisite tracking performance. An anomaly is assumed to occur in the form of loss of effectiveness of the actuator (which may be due to a damage to the control surfaces caused by a sudden change in environmental conditions or a compromised engine due to bird strikes). The trading action proposed in [20] is for the pilot to step in and take over from the autopilot, based on the pilot's perception that the automation is unable to cope with the anomaly. This perception is based on the CfM of the actuator, and when it exceeds a certain threshold, the pilot is proposed to take over control. A well known model of the pilot in [3, 4, 5] is utilized to propose the specific sequence of control actions that the pilot takes once they take over. It is shown through simulation studies that when the pilot carries out this sequence of perception and control tasks, the effect of anomaly is contained, and the tracking performance is maintained at a satisfactory level. A slight variation of the above trading role is reported in [21], where instead of the 'autopilot is active→anomaly occurs→pilot takes over' sequence, the pilot transfers control from one autopilot to a more advanced autopilot following the perception of an anomaly. It is argued that even if an advanced autopilot is used all the time, a shared control architecture is found to be more effective since it makes use of the best capabilities of both the human operator and the automation.

The SCA2 architecture utilized in [22] differs from SCA1, as mentioned above, as the trading action from the autopilot to the pilot is replaced by a supervisory action by the pilot. In addition to using CfM, this architecture utilizes a second principle from cognitive engineering denoted as Graceful Command Degradation (GCD). GCD is proposed as an inherent metric adopted by humans [6] that will allow the underlying system to function so as to retain a target CfM. As the name connotes, GCD corresponds to the extent to which the system is allowed to relax its performance goals. When subjected to anomalies, it is reasonable to impose a command degradation; the greater this degradation, the larger the reserves that the system will possess when recovered from the anomaly. A GCD can then be viewed as a control variable that is tuned so as to permit a system to reach its targeted CfM. The role of tuning this variable so that the desired CfM is retained by the system is relegated to the pilot in [22]. In particular a parameter μ is transferred to the autopilot from the autopilot, which is shown to result in an ideal trade-off between the CfM and GCD by the overall closed-loop system with SCA2.

The subjects used in the human-in-the-loop simulations include an airline pilot, who is also a flight instructor, with 2600 hours of flight experience, as well as human subjects who were trained in a systematic manner by the experiment designer. The details of the training is explained in the Section "Validation with Human in the Loop Simulations". It is shown that the SCA1 in [20] and SCA2 in [22] indeed lead to better performance as conjectured therein when the human expert carries out their assigned roles in the respective architectures. The resulting solution therefore is an embodiment of an efficient cyber-physical human system, a topic that is of significant interest of late.

2.1 Autopilot Models

In this section, we describe the technical details related to the autopilot discussed in [20] and [22].

2.1.1 Dynamic Model of the Aircraft

Since the autopilot in [22] is assumed to be determined using feedback control, the starting point is the description of the aircraft model, which has the form

$$\begin{aligned} \dot{x}(t) &= Ax(t) + B\Lambda_f u(t) + d + \Phi^T f(x), \\ y(t) &= Cx(t) \end{aligned} \tag{2.1}$$

where $x \in \mathbb{R}^n$ and $u \in \mathbb{R}^m$ are deviations around a trim condition in aircraft states and control input, respectively, d represents uncertainties associated with the trim condition, and the last term $\Phi^T f(x)$ represents higher order effects due to nonlinearities. A is a $(n \times n)$ system matrix and B is a $(n \times m)$ input matrix, both of which are assumed to be known, with (A, B) controllable, and Λ_f is a diagonal matrix that reflects a possible actuator anomaly with unknown positive entries λ_{f_i}. C is a known matrix of size $(k \times n)$ chosen so that $y \in \mathbb{R}^k$ corresponds to an output vector of interest. It is assumed that the anomalies occur at time t_a, so that $\lambda_{f_i} = 1$ for $0 \leq t < t_a$, and λ_{f_i} switches to a value that lies between 0 and 1 for $t > t_a$. It is finally postulated that the higher order effects are such that $f(x)$ is a known vector that can be determined at each instant of time, while Φ is an unknown vector parameter. Such a dynamic model is often used in flight control problems [23].

In the context of anomalies, we explicitly accommodate actuator constraints. In particular, we assume that the u is assumed to be position / amplitude limited and modeled as

$$u_i(t) = u_{\max_i} \mathrm{sat}\left(\frac{u_{c_i}(t)}{u_{\max_i}}\right) = \begin{cases} u_{c_i}(t), & |u_{c_i}(t)| \leq u_{\max_i} \\ u_{\max_i}(t)\mathrm{sgn}\left(u_{c_i}(t)\right), & |u_{c_i}(t)| > u_{\max_i} \end{cases} \tag{2.2}$$

where $u_{\max_i}$ for $i = 1, \ldots, m$ are the physical amplitude limits of actuator i, and $u_{c_i}(t)$ are the control inputs to be determined by the shared control architecture (SCA). The functions $\mathrm{sat}(\cdot)$ and $\mathrm{sgn}(\cdot)$ denote saturation and sign functions, respectively.

2.1.2 Advanced Autopilot Based on Adaptive Control

The control input $u_{c_i}(t)$ will be constructed using an adaptive controller. To specify the adaptive controller, a reference model that specifies the commanded behavior from the plant is constructed and is of the form [24]

$$\begin{aligned} \dot{x}_m(t) &= A_m x_m(t) + B_m r_0(t), \\ y_m(t) &= C x_m(t), \end{aligned} \tag{2.3}$$

where $r_0 \in \mathbb{R}^k$ is a reference input, A_m $(n \times n)$ is a Hurwitz matrix, $x_m \in \mathbb{R}^n$ is the state of the reference model and (A_m, B_m) is controllable, and C is defined as given in (2.1), that is, $y_m \in \mathbb{R}^k$ corresponds to a reference model output. The goal of the adaptive autopilot is then to choose $u_{c_i}(t)$ in (2.5) so that if an error e is defined as

$$e(t) = x(t) - x_m(t), \tag{2.4}$$

all signals in the adaptive system remain bounded with error $e(t)$ tending to zero asymptotically.

The design of adaptive controllers in the presence of control magnitude constraints is first addressed in [25], with guarantees of closed-loop stability through modification of the error used for the adaptive law. The same problem is addressed in [26], using an approach termed *μ-mod adaptive control* where the effect of input saturation is accommodated through the addition of another term in the reference model. Yet another approach based on a closed-loop reference model (CRM) is derived in [27], [28] in order to improve the transient performance of the adaptive controller. The autopilot we propose in this paper is based on both the μ-mod and CRM approaches. Using the control input in (2.2), this controller is compactly summarized as

$$u_{c_i}(t) = \begin{cases} u_{\mathrm{ad}_i}(t), & |u_{\mathrm{ad}_i}(t)| \leq u^{\delta}_{\max_i} \\ \frac{1}{1+\mu}\left(u_{\mathrm{ad}_i}(t) + \mu \mathrm{sgn}\left(u_{\mathrm{ad}_i}(t)\right) u^{\delta}_{\max_i}\right), & |u_{c_i}(t)| > u^{\delta}_{\max_i} \end{cases} \tag{2.5}$$

where

$$u_{\mathrm{ad}_i}(t) = K_x^T(t)x(t) + K_r^T(t)r_0(t) + \hat{d}(t) + \hat{\Phi}^T(t)f(x), \tag{2.6}$$

$$u^{\delta}_{\max_i} = (1-\delta)u_{\max_i}, \quad 0 \leq \delta < 1. \tag{2.7}$$

A buffer region in the control input domain $[(1-\delta)u_{\max_i}, u_{\max_i}]$ is implied by (2.5) and (2.7) and the choice of μ allows the input to be scaled somewhere in between. The reference model is also modified as

$$\dot{x}_m(t) = A_m x_m(t) + B_m\left(r_0(t) + K_u^T(t)\Delta u_{\mathrm{ad}}(t)\right) - Le(t), \tag{2.8}$$

$$\Delta u_{\mathrm{ad}_i}(t) = u_{\max_i}\mathrm{sat}\left(\frac{u_{c_i}(t)}{u_{\max_i}}\right) - u_{\mathrm{ad}_i}(t), \tag{2.9}$$

and $L < 0$ is a constant or a matrix selected such that $(A_m + L)$ is Hurwitz.

Finally, the adaptive parameters are adjusted as

$$\begin{aligned}
\dot{K}_x(t) &= -\Gamma_x x(t) e^T(t) P B, \\
\dot{K}_r(t) &= -\Gamma_r r_0(t) e^T(t) P B, \\
\dot{\hat{d}}(t) &= -\Gamma_d e^T(t) P B, \\
\dot{\hat{\Phi}}(t) &= -\Gamma_f f(x(t)) e^T(t) P B, \\
\dot{K}_u(t) &= \Gamma_u \Delta u_{\text{ad}} e^T(t) P B_m,
\end{aligned} \tag{2.10}$$

where $P = P^T$ is a solution of the Lyapunov equation (for $Q > 0$)

$$A_m^T P + P A_m = -Q, \tag{2.11}$$

with $\Gamma_x = \Gamma_x^T > 0$, $\Gamma_r = \Gamma_r^T > 0$, $\Gamma_u = \Gamma_u^T > 0$. It is noted under the effect of a severe anomaly that controller adapts the control surfaces such that a saturation in the control input is avoided.

The stability of the overall adaptive system specified by (2.1), (2.2), (2.3)-(2.11) is established in [26] when $L = 0$. The stability of the adaptive system, when no saturation inputs are present, is also established in [28]. A very straightforward combination of the two proofs can be easily carried out to prove that when $L < 0$ the adaptive system considered in this paper has globally bounded solutions if the plant in (2.1) is open-loop stable and bounded solutions for an arbitrary plant if all initial conditions and the control parameters in (2.10) lie in a compact set.

The adaptive autopilot in (2.5)-(2.11) provides the required control input, u, in (2.1) as a solution to the underlying problem. The autopilot includes several free parameters including μ in (2.5), δ in (2.7), the reference model parameters A_m, B_m, L in (2.8) and the control parameters $K_x(0)$, $K_r(0)$, $K_u(0)$, $\hat{d}(0)$, $\hat{\Phi}(0)$ in (2.10). As will be seen in the next section, the parameters δ and μ are related to CfM and GCD.

2.1.2.1 Quantification of CfM, GCD and Trade-offs

The control input u_{c_i} in (2.5) is shaped by two parameters δ and μ, both of which help tune the control input with respect to its specified magnitude limit

$u_{\max_i}$. We use these two parameters in quantifying CfM, GCD, and the trade-offs between them as follows.

CfM: As mentioned earlier, qualitatively, CfM corresponds to a system's reserved capacity, which we quantitatively formulate in the current context as the distance between a control input and its saturation limits. In particular, we define CfM as

$$\mathrm{CfM} = \frac{\mathrm{CfM}^R}{\mathrm{CfM}_d}, \tag{2.12}$$

where

$$\begin{aligned} \mathrm{CfM}^R &= \mathrm{rms}\left(\min_i(c_i(t))\right)\Big|_{t_a}^{T}, \\ c_i(t) &= u_{\max_i} - |u_i(t)|, \end{aligned} \tag{2.13}$$

$c_i(t)$ is the instantaneous available control input of actuator i, $\mathrm{CfM}^{\mathrm{R}}$ is the root mean squared CfM variation and CfM_d, which denotes the desired CfM is chosen as

$$\mathrm{CfM}_d = \max_i\left(\delta u_{\max_i}\right). \tag{2.14}$$

In the above equations, min and max are the minimum and maximum operators over the i^{th} index, rms is the root mean square operator and t_a and T refer to the time of anomaly and final simulation time, respectively. From (2.13), we note that (i) CfM^R has a maximum value $u_{\max}$ for the trivial case when all $u_i(t) = 0$, (ii) a value close to $\delta u_{\max}$ if the control inputs approach the buffer region, and (iii) zero if $u_i(t)$ hits the saturation limit $u_{\max}$. Since $\mathrm{CfM}_d = \delta u_{\max}$, it follows that CfM, the corresponding normalized value, is greater than unity when the control inputs are small and far away from saturation, unity as they approach the buffer region, and zero when fully saturated.

GCD: As mentioned earlier, the reference model represents the commanded behavior from the plant being controlled. In order to reflect the fact that the actual output may be compromised if the input is constrained, we add a term that depends on $\Delta u_{\mathrm{ad}}(t)$ in (2.9) to become nonzero whenever the control input saturates, that is, when the control input approaches the saturation limit, Δu_{ad_i} becomes nonzero, thereby suitably allowing a graceful degradation of x_m from its nominal choice as in (2.8). We denote this degradation as GCD_i and quantify it as:

$$\mathrm{GCD}_i = \frac{\mathrm{rms}(y_{m,i}(t) - r_{0,i}(t))}{\mathrm{rms}(r_{0,i}(t))}, \quad t \in T_0, \tag{2.15}$$

where T_0 denotes the interval of interest, and $y_{m,i}$ and $r_{0,i}$ indicate the i^{th} elements of the reference model output and reference input vectors, respectively. It should be noted that once μ is specified, the adaptive controller automatically scales the input into the reference model through Δu_{ad} and K_u, in a way so that $e(t)$ remains small and the closed-loop system has bounded solutions.

μ: The intent behind the introduction of the parameter μ in (2.5) is to regulate the control input and move it away from saturation when needed. For example, if $|u_{ad_i}(t)| > u^{\delta}_{\mathrm{max}_i}$, the extreme case of $\mu = 0$ will simply set $u_{c_i} = u_{\mathrm{ad}}$, thereby removing the effect of the virtual limit imposed in (2.7). As μ increases, the control input would decrease in magnitude and move towards the virtual saturation limit $u^{\delta}_{\mathrm{max}_i}$, that is, once the buffer δ is determined, μ controls $u_i(t)$ within the buffer region $[(1-\delta)u_{\mathrm{max}_i}, u_{\mathrm{max}_i}]$, bringing it closer to the lower limit with increasing μ. In other words, as μ increases, CfM increases as well in the buffer region. It should also be noted that the buffer region gives the human operator a chance to regulate the control input so that it does not make a sudden jump due to the selection of μ.

It is easy to see from (2.8) and (2.9) that similar to CfM, as μ increases, GCD increases as well. This is due to the fact that an increase in μ increases $\Delta u_{\mathrm{ad}_i}(t)$ which, in turn, increases the GCD. While a larger CfM improves the responsiveness of the system to future anomalies, a lower bound on the reference command is necessary to finish the mission within practical constraints. In other words, μ needs to be chosen so that GCD remains above a lower limit while maintaining a large CfM. We relegate the task of selecting the appropriate μ to the human pilot.

2.1.2.2 Choice of the Reference Model Parameters

In addition to μ and δ, the adaptive controller in (2.2), (2.3)-(2.11) requires the reference model parameters A_m, B_m, L and the control parameters $K_x(0)$, $K_r(0)$, and $K_u(0)$ at time $t = 0$. If no anomalies are present, then $\Lambda_{\text{nom}} = \Lambda_f = I$ which implies that A_m and B_m as well as the control parameters can be chosen as

$$\begin{aligned} A_m &= A + BK_x^T(0), \\ K_r^T(0) &= -(A_m^{-1}B)^{-1}, \\ B_m &= BK_r^T(0), \\ K_u^T(0) &= -A_m^{-1}B, \end{aligned} \tag{2.16}$$

where $K_x(0)$ is computed using a linear–quadratic regulator (LQR) method and the nominal plant parameters (A, B) [29] and $K_r(0)$ in (2.16) is selected to provide unity low frequency DC gain for the closed-loop system. When anomalies occur, $\Lambda_f \neq I$, at time $t = t_a$ and supposing that an estimate $\hat{\Lambda}_f$ is available (since an approximate guess can still be made on the basis of the severity), a similar choice as in (2.16) can be carried out using the plant parameters $(A, B\hat{\Lambda}_f)$ and the relations

$$\begin{aligned} A_m &= A + B\hat{\Lambda}_f K_x^T(t_a), \\ K_r^T(t_a) &= -(A_m^{-1}B\hat{\Lambda}_f(t_a))^{-1}, \\ B_m &= B\hat{\Lambda}_f K_r^T(t_a), \\ K_u^T(t_a) &= -A_m^{-1}B\hat{\Lambda}_f(t_a), \end{aligned} \tag{2.17}$$

with the adaptive controller specified using (2.2)-(2.11) for all $t \geq t_a$. Finally, L is chosen as in [28] and lower parameters $\hat{d}(0)$, $\hat{\Phi}(0)$ are chosen arbitrarily. Similar to μ, we relegate the task of assessing the estimate $\hat{\Lambda}_{f_p}$ to the human pilot as well.

2.1.3 Autopilot Based on Proportional Derivative Control

To investigate shared control architectures, another autopilot that is employed in the closed loop system is the proportional derivative (PD) controller. Assuming a single control input [20], the goal is to control the dynamics [3]

$$Y_p(s) = \frac{1}{s(s+a)}, \tag{2.18}$$

which represents the aircraft transfer function between the input u and an output $M(t)$, and can be assumed to be a simplified version of the dynamics in (1). It can be argued that this is fairly a good approximation of the dynamics since only one axis is considered (see [3, 4]). The input u is subjected to the same magnitude and rate constraints as in (2.2). Considering the transfer function (2.18) between the input u and the output $M(t)$, the PD controller can be chosen as

$$u(t) = K_p(M(t) - M_{\text{cmd}}(t)) + K_r(\dot{M}(t)), \tag{2.19}$$

where M_{cmd} is the desired command signal that M is required to follow. Given the second-order structure of the dynamics, it can be shown that suitable gains K_p and K_r can be determined so that the closed-loop system is stable and for command inputs at low frequencies, a satisfactory tracking performance can be obtained.

It is noted that during the experimental validation studies certain anomalies are introduced to (2.18) in the form of unmodeled dynamics and time delays. Therefore, according to the crossover model [30], the human pilot has to adapt themselves to demonstrate different compensation characteristics, such as pure gain, lead or lag, based on the type of the anomaly. This creates a challenging scenario for the shared control architecture.

2.2 Human Pilot

In this section, we discuss mathematical models of human pilot decision making on the basis of absence and presence of flight anomalies. A great deal of research has been conducted on mathematical human pilot modeling assuming that no failure in the aircraft or no severe disturbances in the environment are present. Since decision making will differ significantly whether the aircraft is under nominal operation or subjected to severe anomalies, the corresponding models are entirely different as well and are discussed separately in what follows.

2.2.1 Pilot Models in the Absence of Anomaly

In the absence of anomalous event(s), mathematical models of human pilot control behavior can be classified according to control-theoretic, physiological and, more recently, machine learning methods [31], [32]. One of the most well known control-theoretic method in the modelling of human pilot, namely, *the crossover model*, is presented in [30] as an assembly of the pilot and the controlled vehicle, for single loop control systems. The open loop transfer function for the crossover model is

$$Y_h(j\omega)Y_p(j\omega) = \frac{\omega_c e^{-\tau_e j\omega}}{j\omega}, \tag{2.20}$$

where $Y_h(j\omega)$ is a transfer function of the human pilot, $Y_p(j\omega)$ is a transfer function of the aircraft, ω_c is the crossover frequency and τ_e is the effective time delay pertinent to the system delays and human pilot lags. The crossover model is applicable for a range of frequencies around the crossover frequency, ω_c. When a 'remnant' signal is introduced to $Y_h(j\omega)$ to account for the nonlinear effects of the pilot-vehicle system, the model is called a quasi-linear model [33].

Other sophisticated quasi-linear models can be found in the literature as *the extended crossover model* [33], which works especially for conditionally stable systems, that is, when a pilot attempts to stabilize an unstable transfer function of the controlled element, $Y_p(j\omega)$, and *the precision model* [33], which treats a wider frequency region than the crossover model. The single loop control tasks are covered by quasi-linear models. They can be extended to multiloop control tasks by the introduction of *the optimal control model* [34], [35].

Another approach in modeling the human pilot is employing the information of sensory dynamics relevant to humans to extract the effect of motion, proprioceptive, vestibular and visual cues on the control effort. An example of this is *the descriptive model* [36] in which a series of experiments are conducted to distinguish the influence of vestibular and visual stimuli from the control behavior. Another example can be given as *the revised structural model* [37] where the human pilot is modeled as the unification of proprioceptive, vestibular and visual feedback paths. It is hypothesized that such cues help alleviate the compensatory control action taken by the human pilot.

It is noted that due to their physical limitations, models such as in (2.20) are valid for operation in a predefined boundary or envelope where the environmental factors are steady and stable. In the case of an anomaly, they may not perform as expected [38].

2.2.2 Pilot Models in the Presence of Anomaly

When extreme events and failures occur, human pilots are known to adapt themselves to changing environmental conditions, which overstep the boundaries of automated systems. Since the hallmark of any autonomous system is its ability to self-govern even under emergency conditions, modeling of the pilot decision-making upon occurrence of an anomaly is indispensable, and examples are present in the literature [3, 4, 5, 20, 21, 22, 39, 40]. In this thesis, we assume that the anomalies can be modeled either as an abrupt change in the vehicle dynamics [3, 4, 5, 20, 21, 40], or a loss of control effectiveness in the control input [22, 39]. In either case, the objective is the modeling of the decision making of the pilot so as to elicit a resilient performance from the aircraft and recover rapidly from the impact of the anomaly. It should be noted that these models are developed using the Capacity for Maneuver (CfM) concept, the details of which are explained in the following sections.

2.2.2.1 Pilot Models Based on Capacity for Maneuver (CfM)

A recent method in modeling of human pilot under anomalous events utilizes the Capacity for Maneuver (CfM) concept [20], [22], [39]. As discussed in the 'Autopilot' section, CfM refers to the remaining range of the actuators before saturation, which quantifies the available maneuvering capacity of the vehicle. It is hypothesized that surveillance and regulation of a system's available capacity to respond to all events help maintain the resiliency of a system, which is a necessary merit to recover from unexpected and abrupt failures or disturbances [9]. We propose two different types of pilot models, both of which use CfM, but in different ways.

Perception trigger: Here, the pilot model is assumed to assess the CfM and implicitly compute a perception gain based on the CfM. The quantification of this gain, K_t, is predicated on CfM^R with the definition as in (2.13). The perception trigger is associated to the gain K_t, which is implicitly computed as in [20]. The perception algorithm for the pilot is

$$K_t = \begin{cases} 0, & |F_0| < 1 \\ 1, & |F_0| \geq 1 \end{cases} \tag{2.21}$$

where

$$\begin{aligned} F_0 &= G_1(s)[F(t)], \\ F(t) &= \frac{\frac{d}{dt}(\text{CfM}^{R_m}) - \mu_p}{3\sigma_p} \\ \text{CfM}^{R_m} &= u_{\max} - \text{rms}(u(t)). \end{aligned} \tag{2.22}$$

$G_1(s)$ is a second order filter introduced as a smoothing and lagging operator into human perception algorithm, $F(t)$ is the perception variable, CfM^{R_m} is a slightly modified version of CfM^R in (2.13), μ_p is the average of $\frac{d}{dt}(\text{CfM}^{R_m})$ and σ_p is the standard deviation of $\frac{d}{dt}(\text{CfM}^{R_m})$, both of which are measured over a nominal flight simulation. The computation of these statistical parameters is further elaborated in section 'Validation of Shared Control Architecture 1'. The hypothesis here is that the human pilot has such a perception trigger, K_t, and when this trigger, $K_t = 1$, the pilot takes over control from the autopilot. In section 'Experimental Validation of SCA1', we validate this perception model.

CfM-GCD Trade-off: Here, the pilot is assumed to implicitly assess the available (normalized) CfM when an anomaly occurs, and decide on the amount of GCD that is allowable so as to let the CfM become comparable to the CfM_d. In other words, we assume that the pilot is capable of assessing the parameter μ and input this value to the autopilot following the occurrence of an anomaly. That is, the pilot model is assumed to take the available CfM as the input and deliver μ as the output. In section 'Experimental Validation of SCA2', we validate this perception model.

2.3 Details of SCA1 & SCA2

The focus of this section is on a shared control architecture that combines the decision making of a pilot and autopilot in flight control. The architecture is invoked under alert conditions, with triggers in place that specify when the decision-making is transferred from one authority to another. The specific alert conditions that we focus on in this paper corresponds to physical anomalies that compromise the actuator effectiveness. The typical roles of the autopilot and the pilot in a flight control problem were described in Sections 'Autopilot' and 'Human Pilot' respectively. In section 'Autopilot', autopilots based on PD control and adaptive control were described, with former designed to ensure satisfactory command following under nominal conditions, and the latter to accommodate parametric uncertainties including loss of control effectiveness in the actuators. In section 'Pilot Models in the Presence of Anomaly', two different models of decision making in pilots were proposed, both based on the monitoring of CfM of the actuators. In this section, we propose two different shared control architectures, using the models of the autopilots and pilots described in the previous sections.

2.3.1 SCA 1: A pilot with a CfM based perception and a fixed-gain autopilot

The first shared control architecture can be summarized as a sequence {autopilot runs, anomaly occurs, pilot takes over}. That is, it is assumed that an autopilot based on PD control as in (2.19) is in place, ensuring a satisfactory command tracking under nominal conditions. The human pilot is assumed to consist of a perception component and an adaptation component. The perception component consists of monitoring CfM^{R_m}, through which a perception trigger F_0 is calculated using (2.22). The adaptation component consists of monitoring the control gain in (2.21), and taking over control of the aircraft when $K_t = 1$. The details of this shared controller and its evaluation using a numerical simulation study can be found in [20]. Figure 2.1 illustrates the schematic of SCA1.

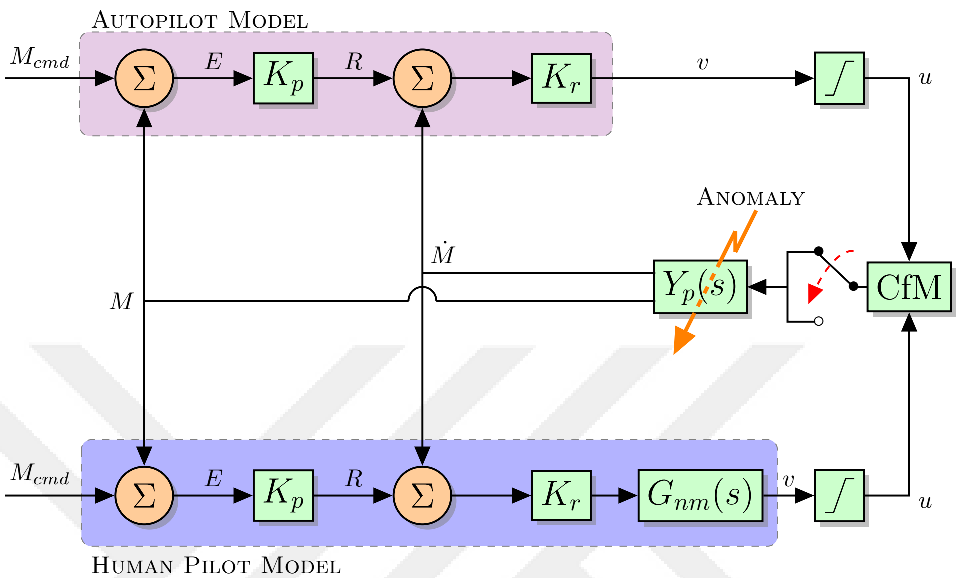

Figure 2.1: Block diagram of the proposed shared control architecture (SCA) 1.

2.3.2 SCA 2: A pilot with a CfM-based decision making and an advanced adaptive autopilot

In this shared control architecture, the role of the pilot is a supervisory one while the autopilot takes on an increased and more complex role. The pilot is assumed to monitor the CfM of the resident actuators in the aircraft following an anomaly. In an effort to allow the CfM to stay close to the CfM_d in (2.14), the command is allowed to be degraded; the pilot then determines a parameter μ which directly scales the control effort through (2.5) and indirectly scales the command signal through (2.8) and (2.9). Once μ is specified by the pilot, then the adaptive autopilot continues to supply the control input using (2.5)-(2.11). If the pilot has high situational awareness, he/she provides $\hat{\Lambda}_{f_p}$ as well, which is an estimate of the severity of the anomaly. The details of this shared controller and its evaluation using a numerical simulation study can be found in [39], [22]. Figure 2.2 shows the schematic of SCA2.

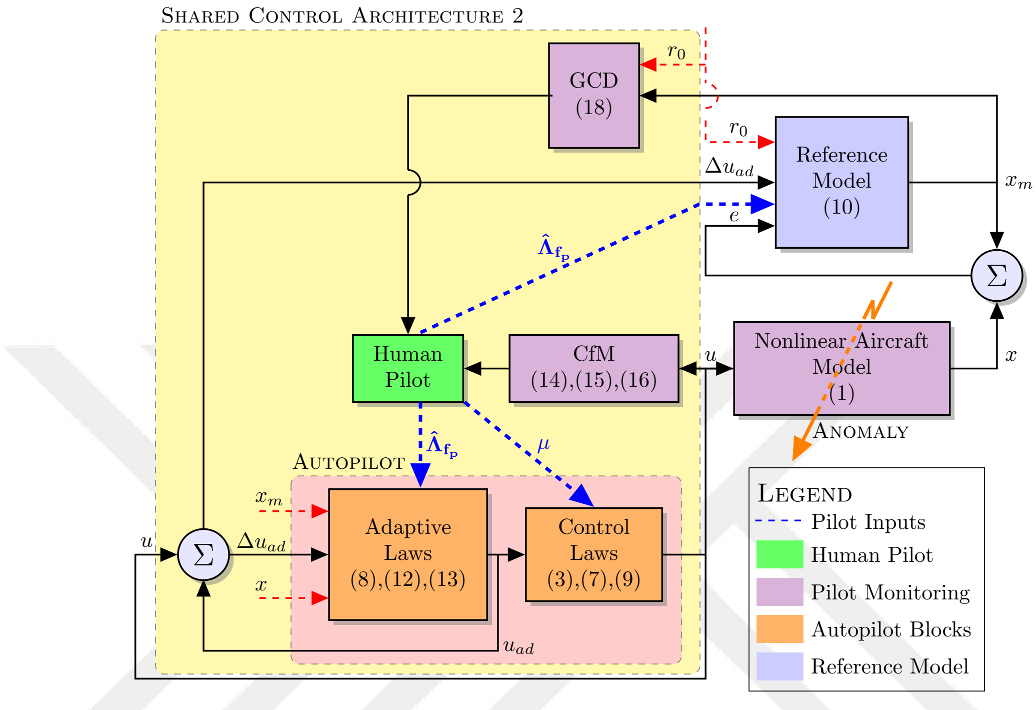

Figure 2.2: Block diagram of the proposed shared control architecture (SCA) 2.

2.4 Validation of SCA1 & SCA2 through Human-In-the-Loop Simulations

The goal in this section is to validate two hypotheses of the human-pilot actions, namely SCA1 and SCA2. Despite the presence of obvious common elements to the two SCAs, of a human pilot, an autopilot, and a shared controller that combines their decision making, the details differ significantly. We therefore describe the validation of these two hypotheses separately in what follows. In each case, we present the validation in the following order: the experimental setup, the type of anomaly, the experimental procedure, details of the human subjects, the pilot-model parameters, results and observations.

Although the experimental procedures used for SCA1 validation and SCA2 validation differ, and therefore explained in separate sections, they use similar principles. To minimize repetition, main tasks can be summarized as follows:

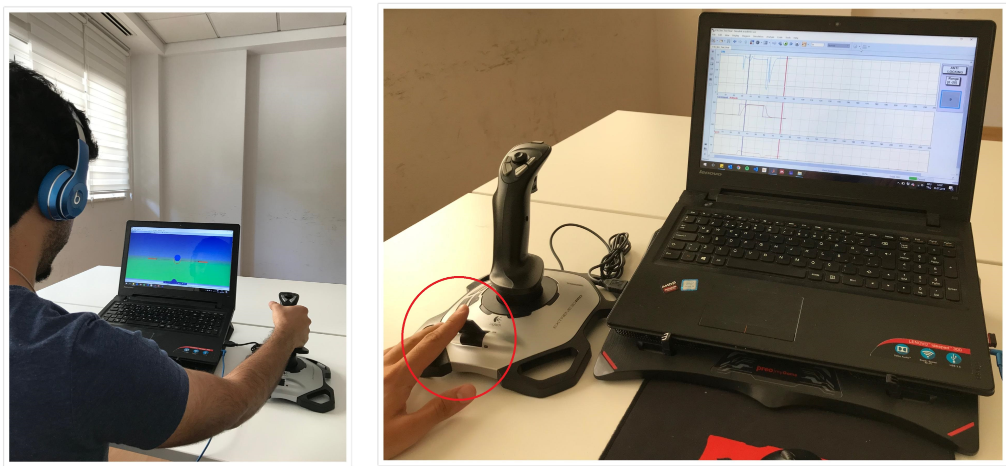

(a) (b)

Figure 2.3: Experimental setups for shared control architecture (SCA) 1 (a) and 2 (b).

The procedure comprises three main phases, namely, *Pilot Briefing*, *Preparation Tests* and *Performance Tests*. In *Pilot Briefing*, the overall aim of the experiment and the experimental setup are introduced. In *Preparation Tests*, the subjects are encouraged to gain practice with the joystick controls. In the last phase, *Performance Tests*, the subjects are expected to conduct the experiments only once in order not to affect the reliability due to learning. Anomaly introduction times are randomized to prevent predictability. As nominal (anomaly-free) plant dynamics, the simpler model introduced in (2.18) is used for SCA1 validation, and a nonlinear F-16 dynamics [41], [42] is used for SCA2 validation. The experiment was approved by the Bilkent University Ethics Committee and an informed consent was taken from each subject before conducting the experiment.

It is noted that during the validation studies, SCA1 and SCA2 are not compared with each other. They are separately validated with different human-in-the-loop simulation settings. However, comparison of SCA1 and SCA2 with each-other can be pursued as a future research direction.

2.4.1 Experimental Validation of SCA1

2.4.1.1 Experimental Setup

The experimental setup consists of a pilot screen and the commercially available pilot joystick Logitech Extreme 3D Pro (see Figure 2.3) with the goal of performing a desktop, human-in-the-loop, simulation. The flight screen interface for SCA1 can be observed in Figure 2.3 - (a) and separately illustrated in Figure 2.4. The orange line with a circle in the middle shows the reference to be followed by the pilot. This line is moved up and down according to the desired reference command, M_{cmd} (see Figure 2.1). The blue sphere in Figure 2.4 represents the nose tip of the aircraft and is driven by the joystick inputs. When the subject moves the joystick, s/he provides the control input, v, which goes through the aircraft model and produces the movement of the blue sphere. The control objective is to keep the blue sphere inside the orange circle, which translates into tracking the reference command. Similarly, the flight screen for SCA2 is shown in Figure 2.3 - (b) and separately illustrated in Figure 2.7. The details on this screen are provided in the 'Validation of the Shared Control Architecture 2' section.

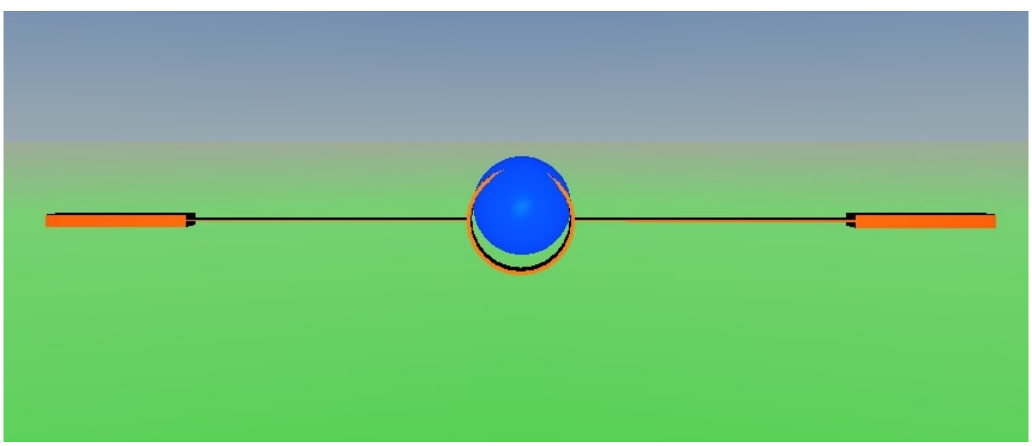

Figure 2.4: Flight screen interface for Shared Control Architecture 1.

2.4.1.2 Anomaly

The anomaly is modeled by a sudden change in vehicle dynamics, from $Y_p^{\text{before}}(s)$ to $Y_p^{\text{after}}(s)$ as in [5], and illustrated in Figure 2.1. Two different flight scenarios, S_{harsh}, and S_{mild}, are investigated, which correspond to a harsh and a mild anomaly, respectively. In the harsh anomaly, it is assumed that

$$Y_{p,h}^{\text{before}}(s) = \frac{1}{s(s+10)}, \quad Y_{p,h}^{\text{after}}(s) = \frac{e^{-0.2s}}{s(s+5)(s+10)}, \tag{2.23}$$

whereas in the mild anomaly, it is assumed that

$$Y_{p,m}^{\text{before}}(s) = \frac{1}{s(s+7)}, \quad Y_{p,m}^{\text{after}}(s) = \frac{e^{-0.18s}}{s(s+7)(s+9)}. \tag{2.24}$$

the specific numerical values of the parameters in (2.23) and (2.24) are chosen so that the pilot action has a distinct effect in the two cases based on their response time. More details of these choices are provided in the following section.

The anomaly is introduced at a certain instant of time, t_a, in the experiment. The anomaly alert is conveyed as sound signal at t_s, following which, the pilots take over control at a time t_{TRT}, after a certain reaction time t_{RT}. Denoting $\Delta T = t_s - t_a$ as the alert time, the total elapsed time from the onset of anomaly to the instant of hitting the joystick button is defined as

$$t_{\text{TRT}} = t_{\text{RT}} + \Delta T. \tag{2.25}$$

2.4.1.3 Experimental Procedure

The experimental procedure consists of three main parts, which are *Pilot Briefing*, *Preparation Tests* and *Performance Tests* (see Figure 2.5).

The first part of the procedure is the *Pilot Briefing*, where the subjects are required to read a pilot briefing to have a clear understanding of the experiment. The briefing consists of six main sections, namely, *Overall Purpose*, *Autopilot*, *Anomaly*, *Experimental Setup*, *Flight Screen* and *Instructions*. In these sections,

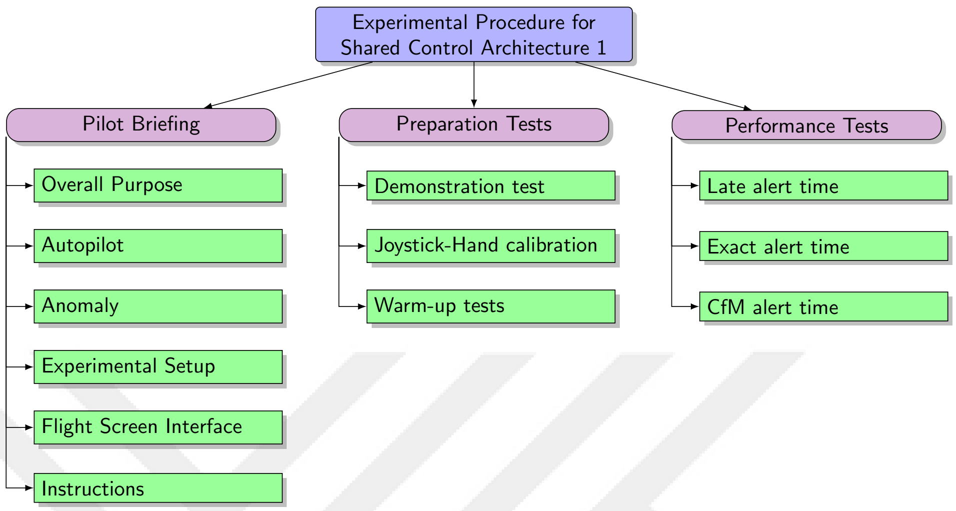

Figure 2.5: Experimental procedure breakdown for the Shared Control Architecture 1.

the main concepts and experimental hardware such as the pilot screen and the joystick lever are introduced to the subject.

The second part is the *Preparation Tests*, in which the subjects are introduced to a demonstration test conducted by the experiment designer to familiarize the subjects to the setup. In this test, the subjects observe the experiment designer follow a reference command using the joystick (See Figure 2.3(a)). They also watch the designer to respond to control switching alert sounds by taking over the control via the joystick. Following these demonstration tests, the subjects are requested to perform the experiment themselves. To complete this part, three preparation tests, each with a duration of 90 seconds are conducted. At the end of each test, the root mean squared error, $\mathrm{e}_{\mathrm{rms}}$, of the subjects is calculated as

$$e_{\mathrm{rms}} = \sqrt{\frac{1}{T_p}\int_{t_a}^{T_p} e(\tau)^2 d\tau}, \tag{2.26}$$

where

$$e(t) = M_{\mathrm{cmd}}(t) - M(t), \tag{2.27}$$

and $T_p = 90\mathrm{s}$. It is expected that the $\mathrm{e}_{\mathrm{rms}}$ in each trial decreases as a sign of learning.

The third is the *Performance Tests*, each with a duration of 180 seconds, which aim at testing the performance of the proposed SCA, in terms of tracking error e_{rms}, CfM^{R_m} and a bumpless transfer metric, ρ, which is calculated by taking the difference of e_{rms} values that are obtained using the 10 second intervals before and after the anomaly. This calculation is performed as

$$\rho = \sqrt{\frac{1}{t_a+10}\int_{t_a}^{t_a+10} e(\tau)^2 d\tau} - \sqrt{\frac{1}{t_a}\int_{t_a-10}^{t_a} e(\tau)^2 d\tau}. \tag{2.28}$$

2.4.1.4 Details of the Human Subjects

The experiment with the harsh anomaly was conducted by 15 subjects (including 1 flight pilot), whereas the one with the a mild anomaly was conducted by 3 subjects (including 1 professional pilot). All subjects were over 18 years old and 4 of the subjects were left-handed, yet this did not bring about any problems, since an ambidextrous joystick was utilized. Some statistical data pertaining to the subjects are given in Table 2.1.

Table 2.1: Statistical data of the subjects in the SCA1 experiment.

Scenario	P	F	μ(Age)	σ(Age)	LH
S_{harsh}	15	1	22.9	3.6	3
S_{mild}	3	0	26.0	5.2	0

P: # of participants, F: female, LH: left-handed

2.4.1.5 Pilot-model parameters

The pilot-model in (2.21)-(2.22) includes statistical parameters μ_p and σ_p, the mean and the standard deviation of the time derivative of CfM^{R_m}, respectively, and the parameters of the filter $G_1(s)$. The filter is chosen as $G_1(s) = \frac{2.25}{s^2+1.5s+2.25}$ so as to reflect the bandwidth of the pilot stick motion. To obtain the other statistical parameters, several flight simulations were run with the PD-control based autopilot in closed-loop and the resulting CfM^{R_m} values were calculated for

180s, both for the harsh and mild anomalies. The time-averaged statistics of the resulting profiles were used to calculate the statistical parameters as $\mu_p = 0.028$, $\sigma_p = 0.038$ for the harsh anomaly, and $\mu_p = 0.091$, $\sigma_p = 0.077$ for the mild anomaly. It should be noted that these statistical parameters are obtained by running an autopilot-controlled flight only.

The pilot model in (2.21)-(2.22) implies that the pilot perceives the presence of the anomaly at the time instant when K_t becomes unity, following which the control action switches from the autopilot to the human pilot. The action of the pilot, based on this trigger, is introduced in the experiment by choosing t_s, the instant of the sound signal, to coincide with the perception trigger. The corresponding $\Delta T = t_s - t_a$, where t_a is the instant when anomaly is introduced, is denoted as a 'CfM-based' one. In order to benchmark this CfM-based switching action, two other switching mechanisms are introduced, one which we define to be 'exact', where $t_s = t_a$, so that $\Delta T = 0$, and another to be 'late', where ΔT is chosen to be significantly larger than the CfM-based one. These choices are summarized in Table 2.2.

Table 2.2: Timeline of Anomalies.

Switch	$t_a[s]$	$t_s[s]$	$\Delta T[s]$
Late	50	55.5	5.5
Exact	50	50	0
CfM-based	50	51.1	1.1

Switch	$t_a[s]$	$t_s[s]$	$\Delta T[s]$
Late	64	74	10
Exact	64	64	0
CfM-based	64	70.2	6.2

2.4.1.6 Results and Observations

We present the results related to the harsh anomaly defined in (2.23) for various alert times transmitted to the subjects. In order to compare the results obtained from the subjects, we also carried out numerical simulation results, where the participants are replaced with the pilot model (2.21)-(2.22), using the same alert times.

Table 2.3: Averaged e_{rms} and CfM^{R_m} values for $\mathrm{S_{harsh}}$.

$\mathrm{S_{harsh}}$	Auto	$\mathrm{Sim_{late}}$	$\mathrm{Exp_{late}}$	$\mathrm{Sim_{exact}}$	$\mathrm{Exp_{exact}}$	$\mathrm{Sim_{CfM\text{-}based}}$	$\mathrm{Exp_{CfM\text{-}based}}$
e_{rms}	478	363	383	319	354	318	348
CfM^{R_m}	8.92	7.93	6.84	7.83	6.80	7.83	7.06

2.4.1.7 Scenario 1: Harsh Anomaly

The results obtained are summarized Table 2.3 using both the tracking error e_{rms} and the corresponding CfM^{R_m}. All numbers reported in Table 2.3 are averaged over all 15 subjects. e_{rms} was calculated using (2.26) with $T_p = 180$s, while CfM^{R_m} was calculated using (2.22) with $u_{\max} = 10$. The statistical variations of both e_{rms} and CfM^{R_m} over the 15 subjects are quantified for all three SCA experiments, for the late, exact, and CfM-based alert times are summarized in Table 2.4. We also calculate the average bumpless transfer metric ρ and its standard error $\sigma_M(\rho)$ for these three cases in Table 2.5. Table 2.5 also provides the average reaction times t_{RT} and average total reaction times t_{TRT} of the subjects.

Table 2.4: Mean, μ and standard error, $\sigma_M = \sigma/\sqrt{n}$, where σ is standard deviation and n is the subject size.

Experiment	μ	σ_M
$\mathrm{Exp_{late}}$	383	16
$\mathrm{Exp_{exact}}$	354	15
$\mathrm{Exp_{CfM\text{-}based}}$	348	14

Experiment	μ	σ_M
$\mathrm{Exp_{late}}$	6.84	0.10
$\mathrm{Exp_{exact}}$	6.80	0.12
$\mathrm{Exp_{CfM\text{-}based}}$	7.06	0.11

Table 2.5: Averaged bumpless transfer metric, ρ, standard error, $\sigma_M(\rho) = \sigma(\rho)/\sqrt{n}$, where σ is standard deviation of ρ and n is the subject size, and averaged reaction times t_{RT} and total reaction times t_{TRT} for $\mathrm{S_{harsh}}$.

Switch	ρ	$\sigma_M(\rho)$	t_{RT} [s]	t_{TRT} [s]
Late	216	4.27	1.07	6.64
Exact	82	1.37	0.98	0.98
CfM-based	26	0.72	0.99	2.12

2.4.1.8 Observations

The first observation from Table 2.3 is that the $e_{\rm rms}$ for the CfM-based case is at least 25% smaller than the case with the autopilot alone. The second observation is that among the shared control architecture experiments, the one with the CfM-based alert time has the smallest tracking error while the one with the late alert time has the largest tracking error. However, it is noted that the difference between the exact and CfM-based cases is not significant.

The third observation from Table 2.3 is that CfM-based control switching from the autopilot to the pilot not only provides the smallest tracking error, but also the largest CfM^{R_m} value compared to other switching strategies. This can also be observed in Figure 2.6, where CfM^{R_m} values, averaged over all subjects, are provided for different alert times. As noted earlier, the large CfM^{R_m} value of the autopilot results from inefficient use of the actuators which manifests itself with a large tracking error. The final observation, which comes from Table 2.5, is that among different alert times, the one with the CfM-based alert time provides the smoothest transfer of control, with a bumpless transfer metric of $\rho = 26$, while the late-alert provides $\rho = 216$ and the exact alert gives $\rho = 82$. These observations imply the following: The pilot re-engagement after an anomaly should not be delayed until it becomes too late, which corresponds to a late-alert switching strategy. At the same time, immediate pilot action right after the anomaly detection might not be necessary either, which is indicated by the fact that the bumpless transfer metric and the CfM^{R_m} values for the CfM-based switching case is better than the exact-switching case. Instead, monitoring the CfM^{R_m} information carefully may be the appropriate trigger for the pilot to take over.

2.4.1.9 Scenario 2: Mild Anomaly

The averaged $e_{\rm rms}$ (scaled by 10^4) and CfM^{R_m} values for this case are given in Table 2.6. The averaged bumpless transfer metric ρ, its standard error $\sigma_M(\rho)$, the average reaction times $t_{\rm RT}$ and the average total reaction times $t_{\rm TRT}$ are presented

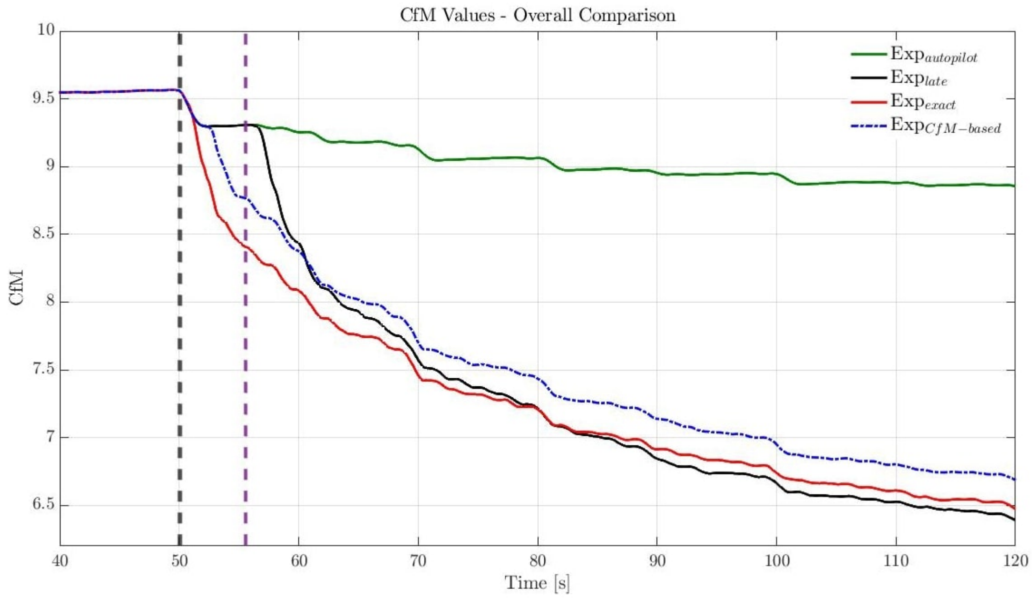

Figure 2.6: CfM^{R_m} variation for the autopilot and all the alert timing mechanisms.

in Table 2.7. The statistical variations of these metrics over the 3 subjects are shown in Table 2.8.

Table 2.6: Averaged e_{rms} and CfM^{R_m} values for $\mathrm{S}_{\mathrm{mild}}$.

$\mathrm{S}_{\mathrm{mild}}$	Auto	$\mathrm{Sim}_{\mathrm{late}}$	$\mathrm{Exp}_{\mathrm{late}}$	$\mathrm{Sim}_{\mathrm{exact}}$	$\mathrm{Exp}_{\mathrm{exact}}$	$\mathrm{Sim}_{\mathrm{CfM\text{-}based}}$	$\mathrm{Exp}_{\mathrm{CfM\text{-}based}}$
e_{rms}	408	281	259	297	236	243	217
CfM^{R_m}	8.78	7.90	7.75	7.64	7.55	8.13	7.79

2.4.1.10 Observations

Similar to the harsh anomaly case, pure autopilot control results in the largest tracking error in the case of a mild anomaly. Also similar to the harsh anomaly case, pilot engagement based on CfM^{R_m} information produces the smallest tracking error, although the difference between the exact switching and CfM-based switching is not significant. However, in terms of preserving CfM^{R_m}, Table 2.8 shows that no significant differences between different switching times can be detected, due to wide spread (high standard error) of the results. The same conclusion can be drawn for the bumpless transfer metric. One reason for this can

Table 2.7: Averaged bumpless transfer metric ρ, standard error $\sigma_M(\rho) = \sigma(\rho)/\sqrt{n}$, where σ is standard deviation of ρ, and n is the subject size, averaged reaction time t_{RT}, and total reaction time t_{TRT} for the experiment with a mild anomaly, $\mathrm{S}_{\mathrm{mild}}$.

Switch	ρ	$\sigma_M(\rho)$	t_{RT} [s]	t_{TRT} [s]
Late	196	3.23	1.06	11.06
Exact	209	8.88	1.02	1.02
CfM-based	203	2.87	0.95	7.20

Table 2.8: Mean, μ and standard error, $\sigma_M = \sigma/\sqrt{n}$, where σ is the standard deviation and n is the subject size, of e_{rms} (on the left) and CfM^{R_m} (on the right), for Scenario 2 with a mild anomaly.

Experiment	μ	σ_M
$\mathrm{Exp}_{\mathrm{late}}$	259	19
$\mathrm{Exp}_{\mathrm{exact}}$	236	21
$\mathrm{Exp}_{\mathrm{CfM\text{-}based}}$	218	14

e_{rms}

Experiment	μ	σ_M
$\mathrm{Exp}_{\mathrm{late}}$	7.75	0.15
$\mathrm{Exp}_{\mathrm{exact}}$	7.55	0.17
$\mathrm{Exp}_{\mathrm{CfM\text{-}based}}$	7.61	0.19

CfM^{R_m}

be the low sample size, 3, in this experiment. One conclusion that can be drawn from these results is that although CfM-based switching shows smaller tracking errors compared to the alternatives, the advantage of the proposed SCA in the presence of mild anomaly is not as prominent as in the case of harsh anomaly.

2.4.2 Experimental Validation of SCA2

Unlike the SCA1, where the pilot took over control from the autopilot when an anomaly occurred, in SCA2, the pilot plays more of an advisory role, directing the autopilot that remains operational throughout. In particular, the pilot provides appropriate values μ and sometimes $\hat{\Lambda}_{f_p}$ as well.

2.4.2.1 Experimental Setup

Contrary to the SCA1 case, here the subjects use the joystick only to enter the μ and $\hat{\Lambda}_{f_p}$ values using the joystick lever. The flight screen that the subjects see is shown in Figure 2.7. There are three subplots, which are normalized $c_i(t)$ (top), reference command (r_0) tracking (middle) and the evolution of graceful command degradation (GCD) (bottom). The horizontal black line in the CfM variation subplot corresponds to the upper bound of the virtual buffer, $[0,\ \delta] = [0,\ 0.25]$. The small rectangle at the upper right serves the purpose of showing the amount of the μ input, entered via the joystick lever. In this rectangle, the title 'Anti Locking' is used to emphasize the purpose of the μ input, which is preventing the saturation/locking of the actuators. There is also another region in this rectangle called the 'Range', which shows the limits of this input.

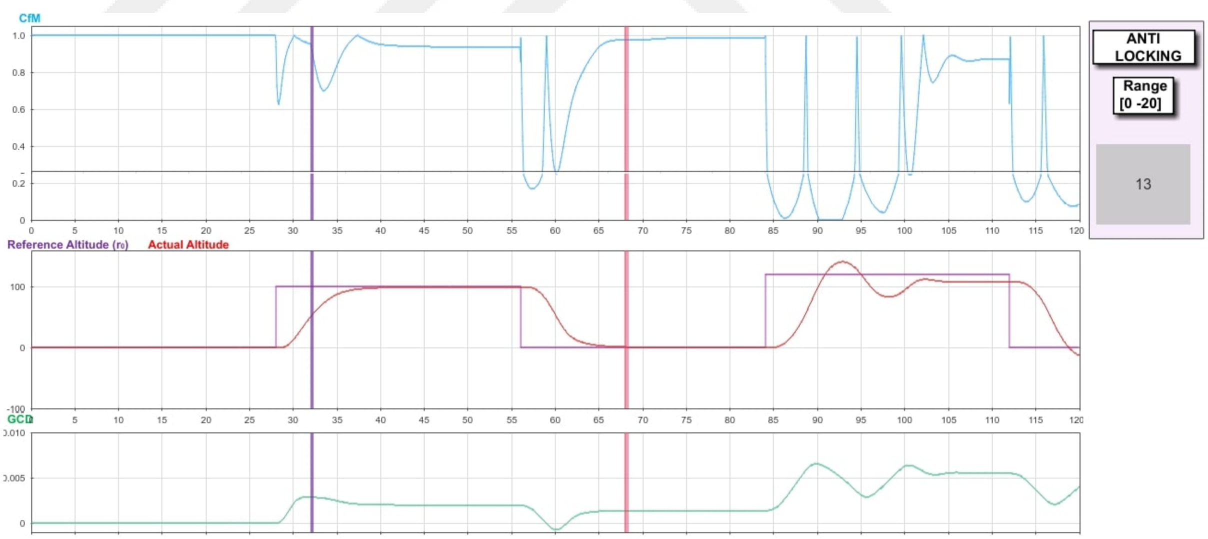

Figure 2.7: Flight screen interface for Shared Control Architecture 2.

In the snapshot of the pilot screen shown in Figure 2.7, a scenario with two anomalies introduced at $t_{a_1} = 32$s and $t_{a_2} = 68$s is shown. The instant of anomaly occurrences are marked with vertical lines, the colors of which indicate the severity of the anomaly. The subjects are trained to understand and respond to the severity and the effect of the anomalies by monitoring the colors, CfM information and the tracking performance. The details of subject training are provided in the 'Experimental Procedure' section.

2.4.2.2 Anomaly

The anomaly considered in this experiment is loss of actuator effectiveness indicated by Λ_f in (2.1). Λ_f is a (2×2) diagonal matrix with equal entries that are between 0 and 1, where 0 corresponds to complete actuator failure and 1 corresponds to no failure. In the experiments, two anomalies are introduced at times $t = t_{a_1}$ and $t = t_{a_2}$. Consequently, the diagonal entries of Λ_f vary as

$$\lambda_{f_i} = \begin{cases} 1, & t < t_{a_1} \\ 0 < \lambda_{f_1} < 1, & t_{a_1} \leq t < t_{a_2} \\ 0 < \lambda_{f_2} < 1, & t_{a_2} \leq t \end{cases} \tag{2.29}$$

where λ_{f_i} refers to the diagonal entries for the i^{th} anomaly introduction. The anomaly injections are communicated to the subjects with colored vertical lines appearing on the pilot screen, as shown in Figure 2.7, together with sound alerts. Three anomalies with different severities are used during the experiments. The anomaly severity quantities are $\Lambda_f = 0.3$ (low), 0.2 (medium) and 0.15 (high), and these are communicated through green, purple and maroon colored vertical lines, respectively. (See Figure 2.7 where a sample experiment is shown with medium and high severity anomalies.)

2.4.2.3 Experimental Procedure

As in SCA1, the experimental procedure consists of three parts, *Pilot Briefing*, *Input Training* and *Performance Test*. (See Figure 2.8 for a schematic). The first part of the procedure is the *Pilot Briefing*, in which the subjects are demanded to read a pilot briefing to acquire knowledge about the experiment. The briefing consists of four main sections, namely, *Overall Purpose*, *Flight Scenario*, *Flight Screen Interface* and *Instructions*. In these sections, the main concepts and the experimental setup are covered by the experiment designer.

The second part is the *Input Training*, in which the subjects are first introduced to the joystick lever, which they are required to use to enter the μ input (See Figure 2.3). By properly moving the lever, an integer value of μ, ranging

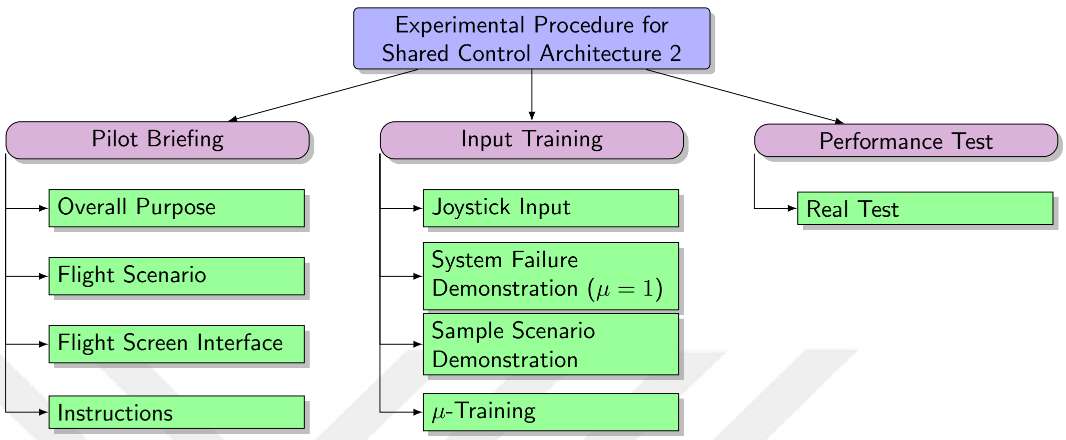

Figure 2.8: Experimental procedure breakdown for the Shared Control Architecture 2.

from 1 to 20, can be given to the controller. Following this, a demonstration test is conducted by the experiment designer. In this test, a sample scenario with two anomalies is run, where the input μ is fixed to its nominal value of $\mu = 1$, throughout the flight. It is explicitly shown that 1) the actuators reaches their saturation limit, and thus the CfM becomes zero, many times during the flight, which jeopardizes the aircraft stability, 2) it takes for the altitude, h, a long time to recover to follow the reference command, and 3) a certain graceful command degradation occurs to relax the performance goals. Following the demonstration test, another sample scenario is run by the designer, in which suitable μ values are provided upon occurrence of the anomalies. Different from the previous demonstration, it is pointed out that 1) with a proper μ, CfM can be kept away from zero and 2) GCD is kept minimal. By this demonstration, the subjects are expected to appreciate that suitable μ inputs help the autopilot recover from severe anomalies in an efficient and swift manner.

Finally, a μ-input-training is performed on the subjects. Six scenarios are introduced to the participants in an interactive manner, by which they learn how to be involved in the overall control architecture.

As a first step, three scenarios with single anomalies are considered. In each severity of the anomaly, an optimal μ, which trades off CfM with GCD, is conveyed to the subjects. Upon doing this, attention is drawn to the fact that each anomaly causes a certain sharp drop in the CfM variation. In other words, more drastic drops occur in CfM with the increase in the severity of anomaly. Following this, three other scenarios with two successive anomalies are studied. It is noted by the combination of different anomalies that nonlinear effects are present in the flight simulation; that is, the μ values corresponding to single anomalies are no longer effective when the anomalies are combined. In both the training and the performance tests, the anomaly severity estimation $\hat{\Lambda}_{f_p}$ input is automatically fed to the controller with an error of 0.2 in absolute value. Then, to compare the effect of this estimation input, we compare two pilot types where the estimation is not provided in one case and provided in the other.

The third part is the *Performance Test*, in which the subjects are expected to handle a combination of a highly severe anomalies ($\Lambda_{f_1} = 0.20$ and $\Lambda_{f_2} = 0.15$) in a flight simulation. They are expected to give suitable μ values on the basis of the training they obtain. Also, in both the training and the performance tests, the introduction of anomaly times are chosen to be completely random to prevent the subjects from making a guess whether or not the anomaly is about to happen. The set of tasks to be tackled by the subjects is summarized as a flowchart in Figure 2.9. These tasks are explained interactively during the sample scenario demonstration (see Figure 2.8), where the subjects have the opportunity to practise the steps in controlling the flight simulation.

2.4.2.4 Details of the Human Subjects

The experiment was performed by 10 subjects all of whom attended the previous experiment. This choice was made deliberately since the subjects of the previous experiment had an acquaintance with the autopilot and shared control concepts. For this reason, the pilot briefing regarding this experiment was written in a tone that the subjects were already familiar with these basic notions. The average age of the participants was 24.2 with a standard deviation of 1.8.

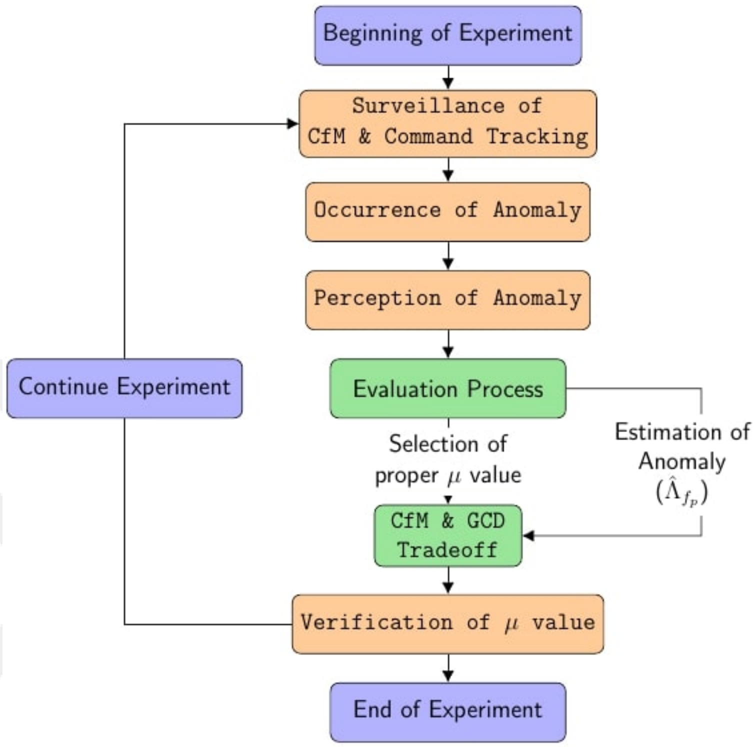

Figure 2.9: Algorithm of pilot tasks.

2.4.2.5 Results and Observations

The autopilots consist of an adaptive controller as in [22], which has no apparent interface with the autopilot, a μ-mod adaptive controller with a fixed value of $\mu = 50$, and an optimal controller. The numerical results averaged over 10 subjects are presented in Table 2.9. The indices in curly brackets $\{h, v\}$ denote the altitude and velocity, respectively. SAP and SUP refer to the 'Situation Aware Pilot' and the 'Situation Unaware Pilot', respectively. SUP provides only a μ input and SAP provides both μ and $\hat{\Lambda}_{f_p}$ to the autopilot. The results for the SUP are obtained by simulating the performance tests by using only the μ inputs provided by the subjects, without their severity estimation inputs $\hat{\Lambda}_{f_p}$. Therefore, to obtain the SUP results, the equation set (2.16) is used, instead of (2.17), while still incorporating the same mu values that were entered by the participants. Furthermore, the tracking performance, γ_i, is calculated as

$$\gamma_i = \text{RMSE}_i^+ - \text{RMSE}_i^-, \qquad (2.30)$$

Table 2.9: Shared Control Architecture (SCA) 2 versus autopilot-only cases.

Method	$\text{RMSE}^{-}_{\{h,v\}}$	$\gamma_{\{h,v\}}$	CfM	GCD
SAP	$\{60, 23\} \times 10^{-4}$	$\{36, 135\} \times 10^{-4}$	1.21	$24.8{\times}10^{-4}$
SUP	$\{60, 23\} \times 10^{-4}$	$\{51, 152\} \times 10^{-4}$	1.16	$24.8{\times}10^{-4}$
Adaptive	$\{24.1, 0.4\}$	$\{0.51, 1.06\}$	0.92	NA
μ-mod	$\{60, 23\} \times 10^{-4}$	$\{0.10, 0.27\}$	0.81	$342{\times}10^{-4}$
Optimal	$\{24.1, 0.4\}$	$\{160.8, 13.8\}$	0.84	NA

where

$$\text{RMSE}^{-}_{i} = \text{rms}(e_i)|_{0}^{t_{a_1}}, \quad \text{RMSE}^{+}_{i} = \text{rms}(e_i)|_{t_{a_1}}^{T}. \tag{2.31}$$

In Figure 2.10, a comprehensive comparison of the SCA2 with autopilot-only cases is given as a matrix of 4×4 plots. Each column presents the results of a specific controller whereas each row shows the comparison of these controllers based on altitude tracking h, velocity tracking V, CfM and elevator control input δ_{el}, respectively. The horizontal dashed red line in the 3rd row shows the buffer limit. The horizontal dashed red and green lines in the 4th row show the limitations posed by $u_{\max}$ and $u^{\delta}_{\max}$ introduced in (2.7).

The results given in Table 2.9 and Figure 2.10 can be summarized as follows: First, it is observed that SCA2, whether with SAP and SUP, outperforms all the other autopilot-only cases. SCA2 provides a higher tracking performance γ, a higher CfM and a lower GCD. Second, SAP shows a better performance than other controllers, including SUP, throughout the simulation run by not only showing a higher tracking performance, but also preventing CfM from reaching zero (saturation point). Third, a quick inspection of the first row of Figure 2.10 shows that both optimal and $\mu-$mod autopilots fail to respond to the second anomaly. This can be explained by the fact that CfM reaches to zero (saturation point) many times, especially in the case of optimal controller. Fourth, the adaptive autopilot shows an acceptable performance up to the second anomaly, but demonstrates degraded behavior with repeated saturation. It is noted that the elevator in the case of adaptive autopilot also hits the saturation point many times and shows a more oscillatory response compared to SAP.

To emphasize the effect of anomaly estimation input $\hat{\Lambda}_{f_p}$, the performances of SCA2 with SAP and SUP are shown separately in Figure 2.11. It is seen that SAP performs better than the SUP in terms of both tracking and CfM metrics. The selection of a suitable μ and the introduction of anomaly estimation, even with an error of 0.2, contribute dramatically to resilient performance, which can also be numerically verified by performance metrics given in Table 2.9.

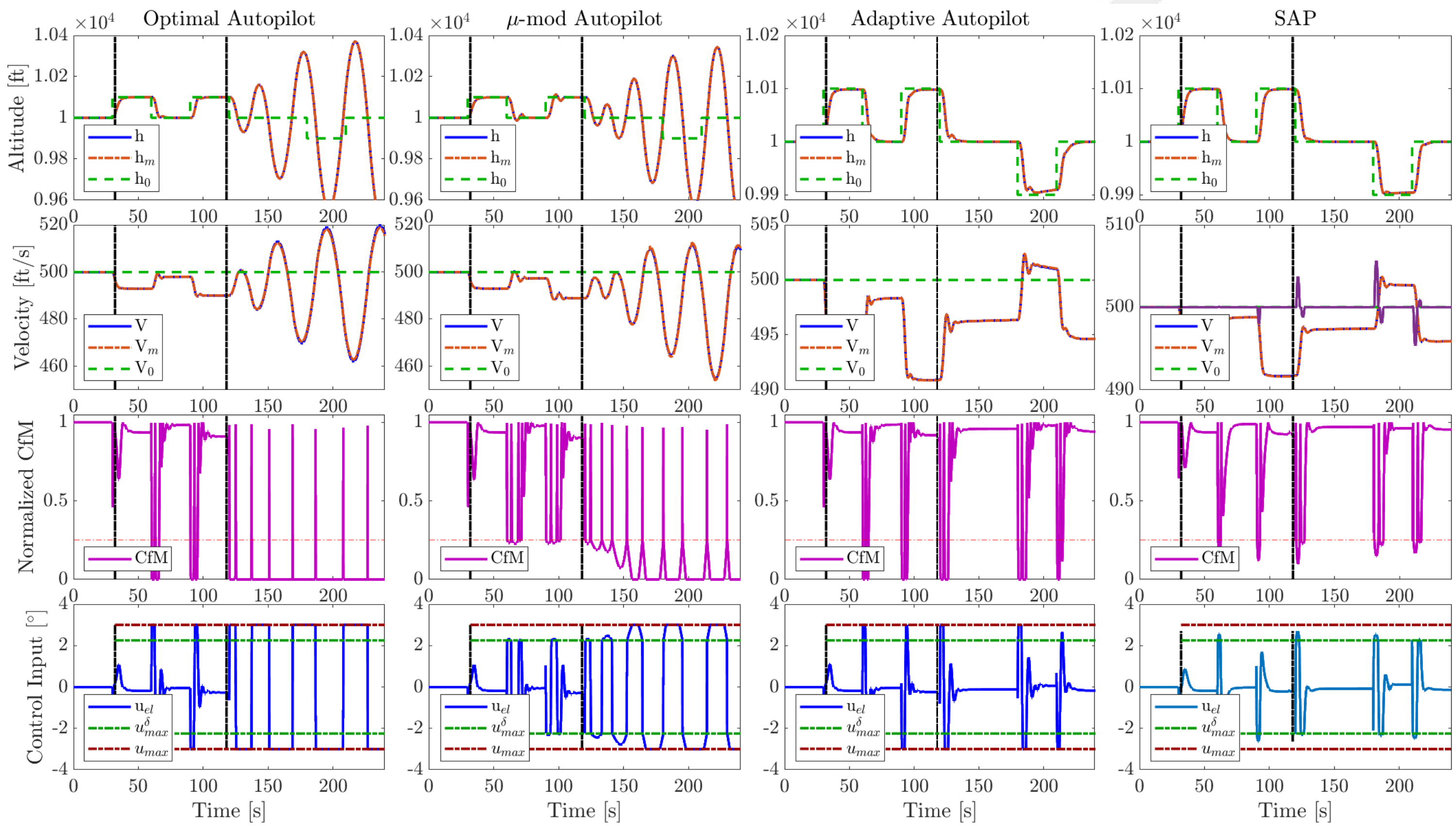

Figure 2.10: SCA2 vs autopilot-only cases. Each column presents the results of a specific controller whereas each row shows the comparison of these controllers based on altitude tracking h, velocity tracking V, CfM and elevator control input δ_{el}, respectively.

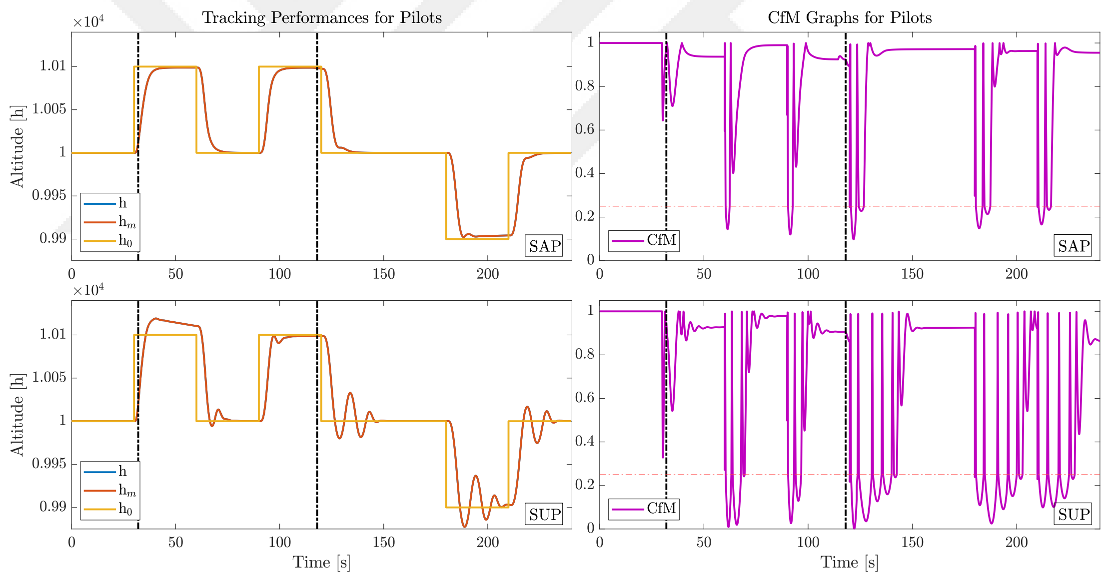

Figure 2.11: Comparison of the SAP and the SUP for the same scenario.

Chapter 3

Adaptive Control and Human-In-The-Loop Simulations of Flexible Quadrotor UAVs

This chapter deals with the control problem of a SCA, where the human pilot provides inputs to an adaptive controller controlling a flexible UAV. This problem is inspired from the control problem of a foldable UAV that is manufactured in Bilkent Miniature Robotics Lab (see Figure 3.1). The control objective is to design a controller that performs the flight mission under severe anomalies, and uncertainties from the user dynamics.

The quadrotor UAVs are conventionally treated as rigid bodies since most of the time flexible dynamics are negligible. However, for quadrotors that are built using very thin and light materials, flexible dynamics cannot be ignored. The preference of these materials contributes significantly to quadrotor design in terms of i) lower manufacturing and maintenance costs, ii) less battery consumption, iii) less fragility due to collision forces, and iv) less proneness to damages during vertical landing.

This chapter introduces an analytical framework for the derivation of hybrid

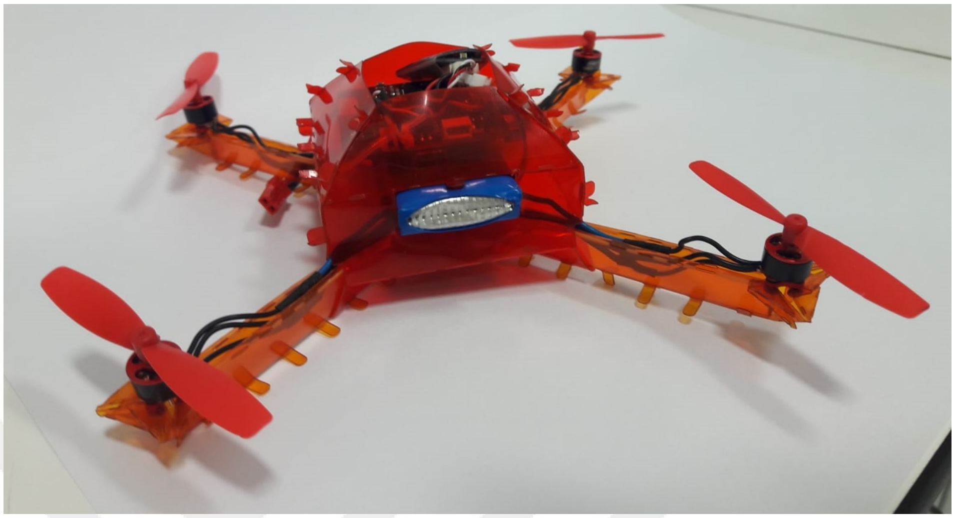

Figure 3.1: The foldable quadrotor UAV manufactured in Bilkent Miniature Robotics Lab

equations of motion of a flexible quadrotor. This approach helps obtain rigid and elastic equations of motion simultaneously, in a decoupled form, which facilitates the controller design. A delay-dependent stability condition is obtained for the overall system dynamics, including the operator with reaction time delay, the adaptive controller and the flexible quadrotor dynamics. This exemplifies the usage of a combined control action in which the human dynamics is also incorporated into the system design.

3.1 Modeling of Elastic Quadrotor Dynamics

In this section, we present the dynamic modeling of a quadrotor UAV considering elastic effects. In obtaining the nonlinear equations of motion, the Lagrangian method is used [43, 44, 45, 46]. Below, we first provide the necessary background for the modeling of unconstrained elastic bodies and then develop the flexible UAV model. We mainly follow the method presented by [47]. However, unlike [47], our equations of motion includes the damping effects. Furthermore, whereas [47] develop a fixed-wing aircraft model, the modeling in this paper is conducted for a quadrotor geometry and loading conditions.

3.1.1 Dynamics of Unconstrained Elastic Bodies

In an unconstrained elastic body (see Figure 3.2), the inertial position $\mathcal{R}_{\mathcal{E}}$ of a mass element ρdV, where ρ is the density and dV is the infinitesimal volume, can be obtained by the summation of its position $\mathcal{R}_{\mathcal{G}}$, relative to a non-inertial body-fixed frame $\mathcal{G}$, and the position $\mathcal{R}_{\mathcal{F}}$ of this body reference frame relative to the inertial frame $\mathcal{F}$ as

$$\mathcal{R}_{\mathcal{E}} = \mathcal{R}_{\mathcal{F}} + \mathcal{R}_{\mathcal{G}}. \tag{3.1}$$

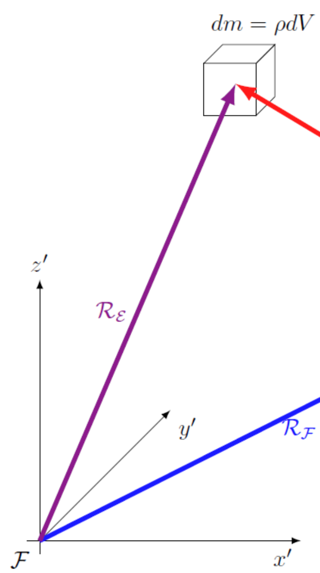

Figure 3.2: Position of a mass element with respect to reference frames

In the usual rigid body formulation, the time rate of change of $\mathcal{R}_{\mathcal{G}}$ is assumed to be zero [48, 49]. This assumption no longer holds true for the elastic body formulation [43]. Denoting $(d/dt)(.)$ as the time derivative with respect to $\mathcal{R}_{\mathcal{F}}$, $(\delta/\delta t)(.)$ as the time derivative with respect to $\mathcal{R}_{\mathcal{G}}$, and ω as the angular velocity of $\mathcal{R}_{\mathcal{G}}$ with respect to $\mathcal{R}_{\mathcal{F}}$, the kinetic and potential energy terms, $\mathcal{T}$ and $\mathcal{U}$, respectively, are obtained as [47]

$$\begin{aligned}\mathcal{T} = \frac{1}{2}\int_V \Bigg\{ & \frac{d\mathcal{R}_{\mathcal{F}}}{dt}\cdot\frac{d\mathcal{R}_{\mathcal{F}}}{dt} + 2\frac{d\mathcal{R}_{\mathcal{F}}}{dt}\cdot\frac{\delta\mathcal{R}_{\mathcal{G}}}{\delta t} + \frac{\delta\mathcal{R}_{\mathcal{G}}}{\delta t}\cdot\frac{\delta\mathcal{R}_{\mathcal{G}}}{\delta t} + 2\frac{\delta\mathcal{R}_{\mathcal{G}}}{\delta t}\cdot(\omega\times\mathcal{R}_{\mathcal{G}}) \\ & +(\omega\times\mathcal{R}_{\mathcal{G}})\cdot(\omega\times\mathcal{R}_{\mathcal{G}}) + 2(\omega\times\mathcal{R}_{\mathcal{G}})\cdot\frac{d\mathcal{R}_{\mathcal{F}}}{dt}\Bigg\}\rho dV,\end{aligned} \tag{3.2}$$

$$\mathcal{U} = -\int_V (\mathcal{R}_\mathcal{F} + \mathcal{R}_\mathcal{G})\, g\rho dV - \frac{1}{2}\int_V \frac{\delta^2 \mathcal{R}_\mathcal{G}}{\delta t^2}\mathcal{R}_\mathcal{G}\rho dV. \tag{3.3}$$

The position of the mass element ρdV relative to the body frame $\mathcal{G}$ can be written as

$$\mathcal{R}_\mathcal{G} = \bar{s} + w(\bar{x}, t), \tag{3.4}$$

where $\bar{s}$ is the constant undeformed length, $w(\bar{x}, t)$ is the relative elastic displacement and $\bar{x}$ is the generalized coordinate on the body frame. Assuming that free vibration modes of the elastic body are given, the relative displacement $w(\bar{x}, t)$ can be expressed in terms of infinitely many mode shapes $W(\bar{x})$ and generalized displacement coordinates $\Upsilon(t)$ as

$$w(\bar{x}, t) = \sum_{j=1}^{\infty} W_j(\bar{x})\Upsilon_j(t). \tag{3.5}$$

Using (3.5) and applying the mean axes theorem [43, 50, 51, 52], (3.2) and (3.3) can be rewritten as

$$\mathcal{T} = \frac{1}{2}m\frac{d\mathcal{R}_\mathcal{F}}{dt}\cdot\frac{d\mathcal{R}_\mathcal{F}}{dt} + \frac{1}{2}\omega^T I\omega + \frac{1}{2}\sum_{j=1}^{\infty} M_j\dot{\Upsilon}_j^2(t), \tag{3.6}$$

$$\mathcal{U} = -mg\mathcal{R}_\mathcal{F} + \frac{1}{2}\sum_{j=1}^{\infty}\bar{\omega}_j^2 M_j\Upsilon_j^2(t), \tag{3.7}$$

where the first, second and the third term in (3.6) are translational, $\mathcal{T}_t$, rotational, $\mathcal{T}_r$ and elastic, $\mathcal{T}_e$, kinetic energy terms, respectively. On the other hand, the first and second term (3.7) are gravitational, $\mathcal{U}_g$, and elastic, $\mathcal{U}_e$, potential energy terms. The term M_j is the generalized mass term and $\bar{\omega}_j$ is the natural frequency corresponding to the j^{th} elastic degree of freedom.

3.1.2 Equations of Motion for an Elastic Quadrotor UAV

The elastic quadrotor UAV consists of three different types of masses, that is, the main body mass m_b, the arm mass m_c and the rotor mass m_r, all of which add up to the total mass $m = m_b + 4m_c + 4m_r$ (See Figure 3.3). The position variable vector and the Euler angles vector pertaining to the center of mass in the body frame are expressed as $\xi = [x, y, z]^T \in \mathbb{R}^3$ and $\upsilon = [\phi, \theta, \psi]^T \in \mathbb{R}^3$, respectively. The inertial angular velocity vector of the center of mass is given by $\omega = [p, q, r]^T \in \mathbb{R}^3$.

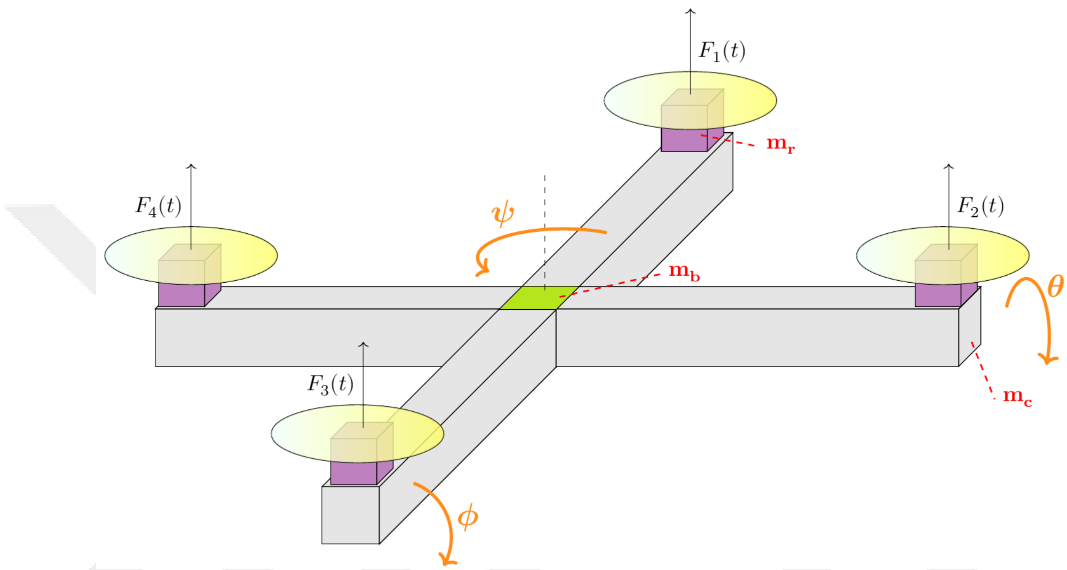

Figure 3.3: A simplified schematic of the elastic quadrotor UAV

The rotation matrix $R^B \in \mathbb{R}^{3\times3}$ that transforms the vectors from $\mathcal{G}$ to $\mathcal{F}$ is given as

$$R^B = \begin{bmatrix} c_\psi c_\theta & c_\psi s_\theta s_\phi - s_\psi c_\phi & c_\psi s_\theta c_\phi + s_\psi s_\phi \\ s_\psi c_\theta & s_\psi s_\theta s_\phi + c_\psi c_\phi & s_\psi s_\theta c_\phi - c_\psi s_\phi \\ -s_\theta & c_\theta s_\phi & c_\theta c_\phi \end{bmatrix}, \tag{3.8}$$

where s_υ and c_υ denote the sine and cosine of the corresponding Euler angle, respectively. The thrust force on the k^{th} rotor is given by

$$F_k = k_t \Omega_k^2, \tag{3.9}$$

where k_t is the thrust factor and Ω_k is the angular velocity of the k^{th} rotor. The total thrust force F_b represented in the body frame $\mathcal{G}$ is

$$F_b = \sum_{k=1}^{4} k_t \Omega_k^2 \begin{bmatrix} 0 \\ 0 \\ 1 \end{bmatrix} = \begin{bmatrix} 0 \\ 0 \\ \sum_{k=1}^{4} k_t \Omega_k^2 \end{bmatrix}. \tag{3.10}$$

F_b represented in the inertial frame $\mathcal{F}$ is given as

$$\mathcal{Q}_\xi = R^B F_b. \tag{3.11}$$

The torques developed due to the rotational velocities of the rotors are calculated as

$$\tau_b = \begin{bmatrix} \tau_\phi \\ \tau_\theta \\ \tau_\psi \end{bmatrix} = \begin{bmatrix} k_t L_c(\Omega_4^2 - \Omega_2^2) \\ k_t L_c(\Omega_3^2 - \Omega_1^2) \\ k_q(-\Omega_1^2 + \Omega_2^2 - \Omega_3^2 + \Omega_4^2) \end{bmatrix}, \tag{3.12}$$

where k_q is the drag factor and L_c is the arm length. Gyroscopic torques are given as

$$\begin{aligned} \tau_g &= -J_r \left[\dot{\upsilon} \times \begin{pmatrix} 0 \\ 0 \\ 1 \end{pmatrix} \right] \Omega_g, \\ \Omega_g &= \Omega_1 - \Omega_2 + \Omega_3 - \Omega_4, \end{aligned} \tag{3.13}$$

where J_r is the moment of inertia of the rotor and Ω_g is the gyroscopic velocity. The total torque, $\mathcal{Q}_\upsilon$, represented in the inertial frame $\mathcal{F}$ is obtained as

$$\mathcal{Q}_\upsilon = \tau_b + \tau_g. \tag{3.14}$$

The control input vector, u, is taken as

$$\begin{aligned} u &= \begin{bmatrix} k_t & k_t & k_t & k_t \\ 0 & -k_t & 0 & k_t \\ -k_t & 0 & k_t & 0 \\ -k_q & k_q & -k_q & k_q \end{bmatrix} \begin{bmatrix} \Omega_1^2 \\ \Omega_2^2 \\ \Omega_3^2 \\ \Omega_4^2 \end{bmatrix}, \\ &= R^{\Omega_s}\Omega_s, \end{aligned} \tag{3.15}$$

where R^{Ω_s} is the corresponding constant transformation matrix, and $\Omega_s = [\Omega_1^2, \Omega_2^2, \Omega_3^2, \Omega_4^2]^T$ is the vector consisting of the squares of rotational velocities. Another useful transformation matrix is the one that converts the force vector $F = [F_1, F_2, F_3, F_4]^T$ into the control input vector u. Multiplying Ω_s with k_t and dividing each element of R^{Ω_s} by k_t, it follows from (3.15) that

$$\begin{aligned} u &= \left(\frac{1}{k_t} R^{\Omega_s} \right) F, \\ &= R^F F, \end{aligned} \tag{3.16}$$

where R^F is the corresponding constant transformation matrix. The generalized coordinates for the elastic body dynamics is given as $q = [\xi^T, \upsilon^T, \Upsilon_j^T]^T \in \mathbb{R}^{(p+6)}$,

$j = 1, 2, \ldots, p$, where p is the number of elastic degrees of freedom, which is infinite in theory but can be truncated to a finite number depending on the level of modeling fidelity. The relation between the rotational velocity vector ω and time rate of change of the Euler angles vector are expressed as

$$\begin{aligned} \omega &= \begin{bmatrix} -s_\theta & 0 & 1 \\ c_\theta s_\psi & c_\psi & 0 \\ c_\theta c_\psi & -s_\psi & 0 \end{bmatrix} \dot{\upsilon}, \\ &= R^\upsilon \dot{\upsilon}, \end{aligned} \tag{3.17}$$

where R^υ is the corresponding transformation matrix. Substituting (3.17) into (3.6), it follows that

$$\mathcal{T}(q, \dot{q}) = \frac{1}{2} m \frac{d\mathcal{R}_\mathcal{F}}{dt} \cdot \frac{d\mathcal{R}_\mathcal{F}}{dt} + \frac{1}{2} \dot{\upsilon}^T R^{\upsilon^T} I R^\upsilon \dot{\upsilon} + \frac{1}{2} \sum_{j=1}^{\infty} M_j \dot{\Upsilon}_j^2(t). \tag{3.18}$$

The Lagrangian consisting of the set of generalized coordinates for the elastic quadrotor UAV can be expressed as

$$\mathcal{L}(q, \dot{q}) = \mathcal{T} - \mathcal{U}. \tag{3.19}$$

The friction term is added exogenously to the formulation in terms of a Rayleigh dissipation function [46, pp. 543-545] as

$$\mathcal{D}(\dot{q}) = \frac{1}{2} \sum_{j=1}^{\infty} \sigma_c \dot{\Upsilon}_j^2(t), \tag{3.20}$$

where the term σ_c is the damping coefficient term. The Lagrangian equation with a dissipation function and generalized forces is given as

$$\frac{d}{dt}\left(\frac{\partial \mathcal{L}}{\partial \dot{q}_i}\right) - \left(\frac{\partial \mathcal{L}}{\partial q_i}\right) + \left(\frac{\partial \mathcal{D}}{\partial \dot{q}_i}\right) = \mathcal{Q}_i, \tag{3.21}$$

where $i = 1, 2, \ldots, (p + 6)$, where Q_i is the generalized force. Using (3.18)-(3.21), the elastic equations of motion can be obtained as

$$\ddot{x} = (\cos(\psi)\sin(\theta)\cos(\phi) + \sin(\psi)\sin(\phi))\,\frac{u_1}{m}, \tag{3.22}$$

$$\ddot{y} = (\sin(\psi)\sin(\theta)\cos(\phi) - \cos(\psi)sin(\phi))\,\frac{u_1}{m}, \tag{3.23}$$

$$\ddot{z} = -g + (\cos(\theta)\cos(\phi))\,\frac{u_1}{m}, \tag{3.24}$$

$$\ddot{\phi} = \dot{\theta}\dot{\psi}\left(\frac{J_y - J_z}{J_x}\right) - \frac{J_r}{J_x}\dot{\theta}\Omega_g + \frac{L_c}{J_x}u_2, \tag{3.25}$$

$$\ddot{\theta} = \dot{\phi}\dot{\psi}\left(\frac{J_z - J_x}{J_y}\right) + \frac{J_r}{J_y}\dot{\phi}\Omega_g + \frac{L_c}{J_y}u_3, \tag{3.26}$$

$$\ddot{\psi} = \dot{\phi}\dot{\theta}\left(\frac{J_x - J_y}{J_z}\right) + \frac{1}{J_z}u_4, \tag{3.27}$$

$$M_j\ddot{\Upsilon}_j(t) + \sigma_c\dot{\Upsilon}_j(t) + \bar{\omega}_j^2 M_j\Upsilon_j(t) = \mathcal{Q}_{\Upsilon_j}(t). \tag{3.28}$$

Remark 1 *The equations of motion comprise a rigid part* (3.22)-(3.27) *and an elastic part* (3.28). *The rigid part of the equations of motions is identical to those of a rigid quadrotor UAV [53, 54]. On the other hand, the elastic part has a form similar to that of an p-many mass spring damper systems, where p is the number of elastic modes.*

3.1.3 Transverse Vibrations of Elastic Arms

In the previous subsection, the equations of motion for an elastic quadrotor were derived. The resulting equations of motion for the elastic part (3.28) are of a relatively simple form, although it is not clear yet what the terms $M_j, \sigma_c, \bar{\omega}_j$ and $\mathcal{Q}_{\Upsilon_j}(t)$ represent in the overall system. In the literature, aeroelastic behavior of flexible aircraft is interpreted as the motion of morphing wings. Upon considering the physical structure of the elastic quadrotor (see Figure 3.3), the arms can be modeled as thin cantilever beams undergoing transverse vibrations (see Figure 3.4) owing to continuous motion and agile maneuvers of the quadrotor.

Although a large body of research is devoted to the modeling of undamped Euler-Bernoulli beams under various boundary conditions, relatively

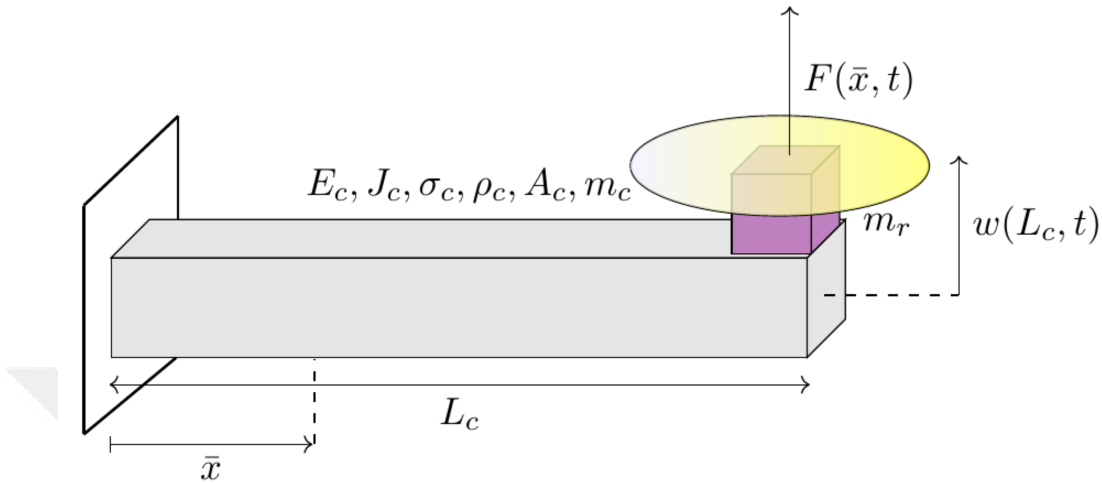

Figure 3.4: An illustration of the elastic quadrotor arm as a cantilever carrying a rotor.

small amount of studies can be found for beams with damping: The damping is formulated as an internal property using the viscoelastic Kelvin-Voigt model by [55] and [56]. On the other hand, a model of a cantilever beam with external damping is developed where a dashpot is attached at the free end [57, 58]. For simplicity, we use the latter approach and write the equations of motion governing the damped Euler-Bernoulli beam presented in Figure 3.4 as

$$E_c J_c \frac{\partial^4 w(\bar{x}, t)}{\partial \bar{x}^4} + \rho_c A_c \frac{\partial^2 w(\bar{x}, t)}{\partial t^2} + \sigma_c \frac{\partial w(\bar{x}, t)}{\partial t} = F(\bar{x}, t), \tag{3.29}$$

where E_c and J_c are the Young's modulus and moment of inertia of the beam, respectively, ρ_c is the density, A_c is the cross-sectional area, σ_c is the damping coefficient of the beam and $F(\bar{x}, t)$ is the concentrated thrust force acting at the beam edge. The solution to the homogeneous part of this equation can be obtained by using (3.5), which consists of the mode shape $W_j(\bar{x})$ and the generalized displacement coordinates $\Upsilon_j(t)$. Since the beam is fixed to the moving main rigid body m_b at one end and carries the rotor mass m_r at the other end (see Figure 3.3), the boundary conditions can therefore be stated as

$$W(0) = 0, \tag{3.30}$$

$$\frac{dW(0)}{d\bar{x}} = 0, \tag{3.31}$$

$$E_c J_c \frac{d^2 W(L_c)}{d^2 \bar{x}} = 0, \tag{3.32}$$

$$E_c J_c \frac{\partial^3 w(L_c, t)}{\partial^3 \bar{x}} = m_r \frac{\partial^2 w(L_c, t)}{\partial^2 t}. \tag{3.33}$$

Taking $F(\bar{x}, t) = 0$, substituting (3.5) into (3.29), and solving it together with (3.30)-(3.33) [44], the transcendental frequency equation is obtained as

$$1 + \frac{1}{\cos \bar{\beta}_j \cosh \bar{\beta}_j} - \bar{m}\bar{\beta}_j (\tan \bar{\beta}_j - \tanh \bar{\beta}_j) = 0, \tag{3.34}$$

$$\beta_j = \sqrt[4]{\frac{\rho_c A_c \bar{\omega}_j^2}{E_c J_c}}, \tag{3.35}$$

where $\bar{\beta}_j = \beta_j L_c$ is the solution of (3.34), β_j is a specific constant obtained from the separation of (3.29) corresponding to the j^{th} natural frequency $\bar{\omega}_j$, and $\bar{m} = m_r/m_c$ denotes the ratio of the rotor mass m_r to the mass of the cantilever beam m_c. For a given j^{th} mode, we can solve for $\bar{\beta}_j$ in (3.34) and calculate a corresponding natural frequency $\bar{\omega}_j$ in (3.35). Following this procedure, we also obtain the mode shape $W_j(\bar{x})$, which can be written as

$$W_j(\bar{x}) = \bar{\gamma}_j \left[(\cos \beta_j \bar{x} - \cosh \beta_j \bar{x}) - \frac{\cos \bar{\beta}_j + \cosh \bar{\beta}_j}{\sin \bar{\beta}_j + \sinh \bar{\beta}_j} (\sin \beta_j \bar{x} - \sinh \beta_j \bar{x}), \right] \tag{3.36}$$

where $\bar{\gamma}_j$ is a normalization constant corresponding to the j^{th} mode (See Appendix A). Having found the mode shapes $W_j(\bar{x})$ in (3.5), we are left to find the solutions of the generalized displacement coordinates $\Upsilon_j(t)$ in (3.28). Applying orthogonality conditions (see Appendix B), it is obtained that

$$\ddot{\Upsilon}_j(t) + \sigma_c' \dot{\Upsilon}_j(t) + \bar{\omega}_j^2 \Upsilon_j(t) = \int_0^{L_c} W_j(\bar{x}) F(\bar{x}, t) d\bar{x}, \tag{3.37}$$

where $\sigma_c' = \sigma_c/(\rho_c A_c)$. It is noted that there is a one-to-one correspondence between (3.28) and (3.37). The generalized mass term M_j in (3.28) refers to $\rho_c A_c$, which is the mass per unit length of the cantilever beam. Considering the right hand side of (3.37) and recalling that $F_k(\bar{x}, t) = F_k(t)\delta(\bar{x} - L_c)$ is a concentrated thrust force for the k^{th} quadrotor arm, $k = \{1, 2, 3, 4\}$, where $\delta(\bar{x})$ is the Dirac's delta function, it can be shown that

$$\int_0^{L_c} W_j(\bar{x}) F_k(t) \delta(\bar{x} - L_c) d\bar{x} = W_j(L_c) F_k(t). \tag{3.38}$$

Substituting (3.38) into (3.37), we obtain that

$$\ddot{\Upsilon}_{kj}(t) + \sigma_c' \dot{\Upsilon}_{kj}(t) + \bar{\omega}_{kj}^2 \Upsilon_{kj}(t) = W_j(L_c) F_k(t), \quad j = 1, 2, .., \infty. \tag{3.39}$$

For each arm of the quadrotor, (3.39) has infinitely many solutions corresponding to each $\bar{\omega}_j$. We choose to take the first three natural frequency values, that is, the variable j takes the values of 1, 2 and 3. The relative displacement $w_k(\bar{x}, t)$ of the arm k at the tip can then be calculated as

$$w_k(L_c, t) = \sum_{j=1}^{3} W_j(L_c)\Upsilon_{kj}(t). \tag{3.40}$$

Using (3.40), we define the corresponding elastic states z_{kj}, $k = \{1, 2, 3, 4\}$, $j = \{1, 2, 3\}$, as

$$z_{kj}(t) = W_j(L_c)\Upsilon_{kj}(t), \tag{3.41}$$

$$\dot{z}_{kj}(t) = W_j(L_c)\dot{\Upsilon}_{kj}(t), \tag{3.42}$$

Multiplying (3.39) with $W_j(L_c)$ and using (3.41) and (3.42), (3.39) can be rewritten as

$$\ddot{z}_{kj}(t) + \sigma'_c \dot{z}_{kj}(t) + \bar{\omega}^2_{kj} z_{kj}(t) = W^2_j(L_c)F_k(t). \tag{3.43}$$

This implies that the tip oscillations at each arm k can be modeled as the summation of solutions of three mass spring damper systems with the same damping coefficient σ'_c but different spring constants $\bar{\omega}^2_{kj}$. Therefore, the elastic states for arm k can be written in a state space form as

$$\dot{z}^k_e = A'_e z^k_e + B'_{ze} F_k, \tag{3.44}$$

where $z^k_e = [z_{k1}, \dot{z}_{k1}, z_{k2}, \dot{z}_{k2}, z_{k3}, \dot{z}_{k3}]^T$, and

$$A'_e = \begin{bmatrix} 0 & 1 & 0 & 0 & 0 & 0 \\ -\bar{\omega}^2_1 & -\sigma'_c & 0 & 0 & 0 & 0 \\ 0 & 0 & 0 & 1 & 0 & 0 \\ 0 & 0 & -\bar{\omega}^2_2 & -\sigma'_c & 0 & 0 \\ 0 & 0 & 0 & 0 & 0 & 1 \\ 0 & 0 & 0 & 0 & -\bar{\omega}^2_3 & -\sigma'_c \end{bmatrix}, B'_{ze} = \begin{bmatrix} 0 \\ W^2_1(L_c) \\ 0 \\ W^2_2(L_c) \\ 0 \\ W^2_3(L_c) \end{bmatrix}. \tag{3.45}$$

Finally, the whole elastic state space formulation can be constructed as

$$\dot{z}_e = A_e z_e + B_{ze} F, \tag{3.46}$$

where $F = [F_1, F_2, F_3, F_4]^T$, and

$$A_e = \begin{bmatrix} A'_e & 0_{6\times 6} & 0_{6\times 6} & 0_{6\times 6} \\ 0_{6\times 6} & A'_e & 0_{6\times 6} & 0_{6\times 6} \\ 0_{6\times 6} & 0_{6\times 6} & A'_e & 0_{6\times 6} \\ 0_{6\times 6} & 0_{6\times 6} & 0_{6\times 6} & A'_e \end{bmatrix}, B_{ze} = \begin{bmatrix} B'_{ze} & 0_{6\times 1} & 0_{6\times 1} & 0_{6\times 1} \\ 0_{6\times 1} & B'_{ze} & 0_{6\times 1} & 0_{6\times 1} \\ 0_{6\times 1} & 0_{6\times 1} & B'_{ze} & 0_{6\times 1} \\ 0_{6\times 1} & 0_{6\times 1} & 0_{6\times 1} & B'_{ze} \end{bmatrix}. \quad (3.47)$$

Using (3.16), the thrust vector can be written in terms of the control input vector u as $F = (R^F)^{-1}u$. Substituting this into (3.46), defining $B_e = B_{ze}(R^F)^{-1}$, and introducing an actuator effectiveness matrix Λ, it is obtained that

$$\dot{z}_e = A_e z_e + B_e \Lambda u. \quad (3.48)$$

Remark 2 *Since the matrix A_e is stable, the subsystem* (3.48) *is bounded-input bounded-states stable. This stability result enables a controller design that is based on rigid body dynamics. However, the designer needs to ensure that 1) control input excitations are not close to the natural frequencies of the elastic modes, and 2) the controller minimizes arm tip oscillations. We discuss these issues in the controller design section below.*

3.2 Controller Design and Human-in-the-Loop Stability Analysis

The overall closed loop control system consisting of an inner and an outer loop is presented in Figure 3.5. The inner loop constitutes the uncertain elastic quadrotor dynamics with a closed loop reference model (CRM) adaptive controller. The human operator exists in the outer loop, where s/he observes the commanded and actual plant states, and produces a reference input for the inner loop. Below, we first explain the CRM adaptive controller design and then provide an overall stability analysis in the presence of the human operator.

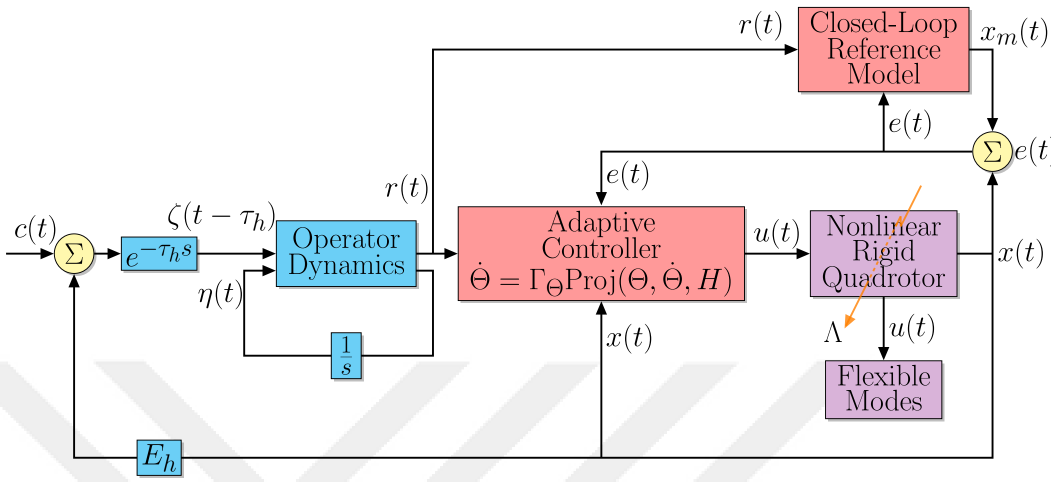

Figure 3.5: Block diagram of the overall control architecture including the operator dynamics.

3.2.1 Controller Design

Nonlinear equations of motion in (3.22)-(3.27) are linearized around a hover position by performing small angle approximations [59]. The resulting equations of motion can be represented as

$$\begin{aligned} \dot{x}_p(t) &= A_p x_p(t) + B_p \Lambda u(t) + B_p \Theta_p^T \Phi_p(x_p(t)) \\ y_p(t) &= C_p x_p(t), \end{aligned} \tag{3.49}$$

where $x_p \in \mathbb{R}^{n_p}$ comprises the position and the Euler angles variables and their corresponding derivatives, $u \in \mathbb{R}^{n_m}$ is the control input, $\Theta_p \in \mathbb{R}^{n_s \times n_m}$ is an unknown weight matrix, $\Phi_p : \mathbb{R}^{n_p} \to \mathbb{R}^{n_s}$ is a known vector of the form $\Phi_p(x_p) = [\Phi_{p_1}(x_p), \Phi_{p_2}(x_p), \cdots, \Phi_{p_s}(x_p)]^T$ of high order nonlinear effects and $y_p \in \mathbb{R}^{n_r}$ is the plant output. Besides, $A_p \in \mathbb{R}^{n_p \times n_p}$ is constant and unknown, $B_p \in \mathbb{R}^{n_p \times n_m}$ is a known constant matrix, with the assumption that (A_p, B_p) is controllable, and $\Lambda \in \mathbb{R}^{n_m \times n_m}$ is an unknown positive definite matrix representing the control effectiveness. The evolution of the elastic states is given in (3.48). The control goal of interest is bounded command tracking in the presence of uncertainties, that is, tracking a reference $r(t) \in \mathbb{R}^{n_r}$ produced by the human pilot (See Figure 3.5). To achieve tracking, a new state vector $e_p \in \mathbb{R}^{n_r}$ is defined as the integral of the tracking error,

$$e_p(t) = \int_0^t [y_p(\varepsilon) - r(\varepsilon)] d\varepsilon, \tag{3.50}$$

and augmented with (3.49), which results in the dynamics

$$\dot{x}(t) = Ax(t) + B\Lambda u(t) + B\Theta_p^T \Phi_p(x_p(t)) + B_m r(t), \tag{3.51}$$

where

$$A = \begin{bmatrix} A_p & 0_{n_p \times n_m} \\ C_p & 0_{n_m \times n_m} \end{bmatrix}, \quad B = \begin{bmatrix} B_p \\ 0_{n_m \times n_m} \end{bmatrix}, \quad B_m = \begin{bmatrix} 0_{n_p \times n_r} \\ -I_{n_r \times n_r} \end{bmatrix}, \tag{3.52}$$

and $x(t) = [x_p(t)^T, e_p(t)^T]^T \in \mathbb{R}^{(n_p + n_m)}$ is the augmented state vector with $n = n_p + n_m$. The control law is determined as

$$u(t) = u_{\text{bl}}(t) + u_{\text{ad}}(t), \tag{3.53}$$

where $u_{\text{bl}}(t) \in \mathbb{R}^{n_m}$ and $u_{\text{ad}}(t) \in \mathbb{R}^{n_m}$ are the baseline and the adaptive control laws, respectively. The baseline controller is given as

$$u_{\text{bl}}(t) = -K^T x(t), \tag{3.54}$$

where $K \in \mathbb{R}^{n \times n_m}$ is a fixed state feedback control gain matrix. We choose this gain such that

$$A_m = A - B\Lambda K^T \tag{3.55}$$

becomes a stable matrix. The reference model is selected as

$$\dot{x}_m(t) = A_m x_m(t) + B_m r(t) - Le(t), \tag{3.56}$$

where $x_m \in \mathbb{R}^n$ is the reference model state vector, $e(t) = x(t) - x_m(t)$ is the tracking error and $L \in \mathbb{R}^{n \times n} < 0$ is a constant matrix such that $(A_m + L)$ is Hurwitz. Substituting (3.53), (3.54) and (3.55) into (3.51), one obtains

$$\dot{x}(t) = A_m x(t) + B_m r(t) + B\Lambda[u_{\text{ad}}(t) + \Theta^T \Phi(x(t))], \tag{3.57}$$

where $\Theta^T = \left[\Lambda^{-1}\Theta_p^T\right] \in \mathbb{R}^{n_m \times n_s}$ is the unknown overall weight matrix and $\Phi^T(x(t)) = \left[\Phi_p^T(x_p(t))\right] \in \mathbb{R}^{(n_s + n)}$ is a vector of high order nonlinear effects. We choose an adaptive control of the form

$$u_{\text{ad}}(t) = -\hat{\Theta}^T \Phi(x(t)), \tag{3.58}$$

where $\hat{\Theta} \in \mathbb{R}^{(n_s+n)\times n_m}$ is the matrix of time-varying adaptive parameters. The adaptive law is given by

$$\dot{\hat{\Theta}} = \Gamma_\Theta \Phi(x(t)) e^T(t) PB, \tag{3.59}$$

where $\Gamma_\Theta \in \mathbb{R}^{[(n_s+n)\times n_m]\times[(n_s+n)\times n_m]}$ is a diagonal positive definite matrix of adaptive gains and $P \in \mathbb{R}^{n\times n}$ is the unique symmetric positive definite solution of the Lyapunov equation

$$(A_m + L)^T P + P(A_m + L) = -Q, \tag{3.60}$$

where $Q \in \mathbb{R}^{n\times n} > 0$ is a positive definite symmetric matrix. To prevent adaptive parameter drifts, the projection algorithm [60, 61, 62, 63, 64] is employed as

$$\dot{\hat{\Theta}} = \Gamma_\Theta \, \mathrm{Proj}(\hat{\Theta}, \Phi(\mathrm{x(t)})\mathrm{e}^{\mathrm{T}}(\mathrm{t})\mathrm{PB}, \mathrm{H}), \tag{3.61}$$

where the projection operator is defined as

$$\mathrm{Proj}(\Theta, Y, H) = \left[\mathrm{Proj}\left(\theta_1, y_1, h_1\right) \ldots \mathrm{Proj}\left(\theta_m, y_m, h_m\right)\right], \tag{3.62}$$

where $\Theta = [\theta_1 \ldots \theta_m] \in \mathbb{R}^{(n_s+n)\times n_m}$, $Y = [y_1 \ldots y_m] \in \mathbb{R}^{(n_s+n)\times n_m}$, and $H = \left[h_1\left(\theta_1\right) \ldots h_m\left(\theta_m\right)\right]^T \in \mathbb{R}^{n_m\times 1}$. The vector form of the projection operator is

$$\mathrm{Proj}\left(\theta_j, y_j, h_j\right) = \begin{cases} y_j - \frac{\nabla h_j(\theta_j)(\nabla h_j(\theta_j))^T}{\|\nabla h_j(\theta_j)\|^2} y_j h_j\left(\theta_j\right) & \text{if } h_j\left(\theta_j\right) > 0 \wedge y_j^T \nabla h_j\left(\theta_j\right) > 0 \\ y_j & \text{otherwise} \end{cases} \tag{3.63}$$

where $h : \mathbb{R}^{n_m} \to \mathbb{R}$ is a convex function and $\nabla h(\theta) = \left(\frac{\partial h(\theta)}{\partial \theta_1} \cdots \frac{\partial h(\theta)}{\partial \theta_{n_m}}\right)^T$. Defining the adaptive parameter estimation error as $\tilde{\Theta} = \hat{\Theta} - \Theta$, and subtracting (3.56) from (3.57), the reference model tracking error can be obtained as

$$\dot{e}(t) = A_m e(t) - B\Lambda\tilde{\Theta}^T \Phi(x(t)) + Le(t). \tag{3.64}$$

Using the Lyapunov function candidate

$$\mathcal{V}(e, \tilde{\Theta}) = e^T(t) P e(t) + \mathrm{tr}[(\tilde{\Theta}^T \Gamma^{-1} \tilde{\Theta})\Lambda], \tag{3.65}$$

it can be shown that

$$\dot{\mathcal{V}}(e(t), \tilde{\Theta}(t)) = -e^{\mathrm{T}}(t) \, \mathrm{Pe}(t) \leq 0. \tag{3.66}$$

This implies that the equilibrium point of (3.59) and (3.64) is stable in the sense of Lyapunov. The convergence of e to zero can typically be shown using Barbalat's Lemma. However, here the lemma is inapplicable, since $\ddot{\mathcal{V}}(e(t), \tilde{\Theta}(t))$ cannot be proven to be bounded, yet. The term $x(t) = e(t) + x_m(t)$ contains the reference model state $x_m(t)$, which can grow unboundedly due to the reference $r(t)$ produced by the human pilot model. For this reason, the dynamics of the outer loop needs to be investigated to determine whether or not $x_m(t)$ and $r(t)$ are bounded.

3.2.2 Outer Loop Dynamics

We use a linear model with a time delay for human operator dynamics, represented as

$$\dot{\eta}(t) = A_h \eta(t) + B_h \zeta(t - \tau_h), \tag{3.67}$$

$$r(t) = C_h \eta(t) + D_h \zeta(t - \tau_h), \tag{3.68}$$

where $\eta(t) \in \mathbb{R}^{n_\eta}$ is the human state vector, $\tau_h \in \mathbb{R}^+$ is the reaction delay, and $A_h \in \mathbb{R}^{n_\eta \times n_\eta}, B_h \in \mathbb{R}^{n_\eta \times n_c}, C_h \in \mathbb{R}^{n_r \times n_\eta}$, and $D_h \in \mathbb{R}^{n_r \times n_c}$ are constant matrices. $r(t) \in \mathbb{R}^{n_r}$ is the reference formed by the human operator (see Figure 3.5). The input to the human dynamics is a feedback error term of the form

$$\zeta(t) = c(t) - E_h x(t), \tag{3.69}$$

where $E_h \in \mathbb{R}^{n_c \times n}$ is a constant matrix that allows to choose a subset of the state $x(t)$ as feedback. Similar human models, containing a linear part and a time delay can also be found in [65, 66, 67]. The analysis in this chapter follows the similar steps used in [68]. Using (3.68) and (3.69), (3.56) and (3.67) can be rewritten as

$$\begin{aligned} \dot{x}_m(t) =& A_m x_m(t) + B_m C_h \eta(t) - B_m D_h E_h [x_m(t - \tau_h) + e(t - \tau_h)] \\ & + B_m D_h c(t - \tau_h) - Le(t), \end{aligned} \tag{3.70}$$

$$\dot{\eta}(t) = A_h \eta(t) - B_h E_h x_m(t - \tau_h) - B_h E_h e(t - \tau_h) + B_h c(t - \tau_h). \tag{3.71}$$

Defining $\mu(t) \triangleq \left[x_m^T(t), \eta^T(t)\right]^T$, (3.70) and (3.71) can be represented as a single delay equation as

$$\dot{\mu}(t) = \mathcal{A}_n \mu(t) + \mathcal{A}_d \mu(t - \tau_h) + \Pi(\cdot), \tag{3.72}$$

where

$$
\begin{aligned}
\mathcal{A}_n &= \begin{bmatrix} A_m & B_m C_h \\ 0_{n_\eta \times n} & A_h \end{bmatrix}, \\
\mathcal{A}_d &= \begin{bmatrix} -B_m D_h E_h & 0_{n \times n_\eta} \\ -B_h E_h & 0_{n_\eta \times n_\eta} \end{bmatrix}, \\
\Pi(\cdot) &= \begin{bmatrix} -Le(t) - B_m D_h E_h e(t-\tau_h) + B_m D_h c(t-\tau_h) \\ -B_h E_h e(t-\tau_h) + B_h c(t-\tau_h) \end{bmatrix}.
\end{aligned}
\tag{3.73}
$$

Since $e(t)$ is shown to be bounded in the previous section and the command $c(t)$ is assumed to be bounded, the matrix $\Pi(\cdot)$ is bounded.

Theorem 3.2.1 *Consider the dynamics given in* (3.72)*. If the real parts of all the infinitely many roots of the equation*

$$
\det\left(sI - \left(\mathcal{A}_n + \mathcal{A}_d e^{-\tau_h s}\right)\right) = 0 \tag{3.74}
$$

have strictly negative real parts, then $\mu(t) \in \mathcal{L}_\infty$ and $\lim_{t\to\infty} e(t) = 0$.

Proof 1 *If all of the roots of the characteristic equation* (3.74) *have strictly negative real parts, then the homogeneous part of* (3.72)*, given as*

$$
\dot{\mu}(t) = \mathcal{A}_n \mu(t) + \mathcal{A}_d \mu(t-\tau_h) \tag{3.75}
$$

is stable. Furthermore, since the forcing term $\Pi(\cdot)$ *in* (3.72) *is bounded, the the solution* $\mu(t)$ *is bounded. This implies that both the reference model state* $x_m(t)$ *and the human state* $\eta(t)$ *are bounded. At this point, it can be shown that the second derivative of the Lyapunov function* (3.65) *is bounded. Hence, with the application of Barbalat's Lemma it can be shown that* $\lim_{t\to\infty} e(t) = 0$.

Remark 3 *Depending on the application, stability limits of the overall system change based on the roots of* (3.74)*. In the following section, we conduct this analysis for our simulation example.*

3.3 Human-In-The-Loop Simulations

In this section, a number of simulations are performed in order to demonstrate the stability and performance characteristics of the human-in-the-loop control system, consisting of the human operator, the controller and the flexible UAV. Below, we first explain the simulation scenario, the controller design details, the stability limits of the operator dynamics and then discuss the simulation results.

3.3.1 Simulation Scenario

In the simulations, the elastic UAV equations of motion introduced in (3.22)-(3.27) and (3.48) are used as the plant model. The human operator is assumed to behave like a proportional integral (PI) controller, with a reaction time delay. This model is consistent with the operator model introduced in (3.67)-(3.69), and can be represented as

$$G_{\mathrm{PI}}(s) = K_p \frac{T_p s + 1}{s} e^{-\tau_h s}, \tag{3.76}$$

where $K_p > 0$ and $T_p > 0$ are model constants, and τ_h is the human operator reaction time delay. The parameters used in the UAV and operator models are given in Table 3.1.

Two types of flight conditions are simulated: operator controlled and autonomous flight. In the operator controlled flight, the human operator's goal is to make the UAV follow a desired altitude command z_d, by producing a corresponding reference input, which is fed to the controller (See Figure 3.5). During this flight mode, the rest of the position and attitude references, x_d, y_d and ψ_d, are created externally. In the autonomous flight mode, all of the reference inputs are created externally and achieved autonomously by the controller, without any interference from the operator. In a simulation of 70 seconds, two anomalies are injected at $t_a = 16s$, which result in loss of control effectiveness of 75% and 50% in the second and third rotors, respectively.

Table 3.1: Elastic UAV Model and Human Operator Parameters

Quadrotor Body	Value	Unit	Arms	Value	Unit	Operator	Value
m	0.5	kg	L_c	0.21	m	K_p	0.59
J_x	4.85×10^{-3}	kgm^2	ρ_c	1370	kgm^3	T_p	0.41
J_y	4.85×10^{-3}	kgm^2	E_c	2.91	GPa	τ_h	0.20
J_z	8.81×10^{-3}	kgm^2					
J_r	3.36×10^{-5}	kgm^2					

3.3.2 Controller Design Details

The baseline controller gain vector K is first calculated based on the nominal plant dynamics. Then, the elements of this vector is decreased by 20% to introduce additional uncertainty. For the design of the adaptive controller, three sets of design parameters need to be determined: Adaptation rates, initial adaptive parameter values and projection boundaries. An empirical approach that assumes that the control parameters reach their ideal values within three time constants is employed to determine the adaptation rates. [69, 70]. This method can mathematically be expressed as

$$\Gamma_{\Theta_{ii}} = \frac{\|\Theta_i\|}{3\tau_m|\bar{r}^2|}, \tag{3.77}$$

where τ_m is the smallest time constant of the reference model A_m and $\bar{r}$ is the maximum value of the reference. Since the ideal control parameter values are unknown, the nominal ideal values (calculated using the nominal plant dynamics) are used instead. It is noted that (3.77) is mainly used as a starting point for fine-tuning the adaptation rates. The initial conditions of all the adaptive control parameters are set to zero. Finally, the projection boundaries are selected by observing the variation of controller parameters during simulations.

3.3.3 Stability Limits

As stated in Theorem 3.2.1, once the CRM adaptive controller is designed as given in (3.53)-(3.63), the stability of the overall system is determined by the roots of the characteristic polynomial presented in (3.74). We use the DDE-BIFTOOL [71] to find the rightmost root, among infinitely many of them, of this polynomial for the simulation example. Specifically, we are interested in the effect of the operator parameters K_p and T_p in (3.76) on the stability of the overall system. Figure 3.6 shows the location of the rightmost root of the characteristic polynomial (3.74) for different values of K_p and T_p. The red areas in the figure represent the unstable regions. It can be argued that the system can be swept into the unstable region for moderately high values of T_p. In addition, the relatively small patch of instability around $K_p = 0.6$ and $T_p = 0.07$ shows the possibility of unexpected system behavior due to operator time-delays.

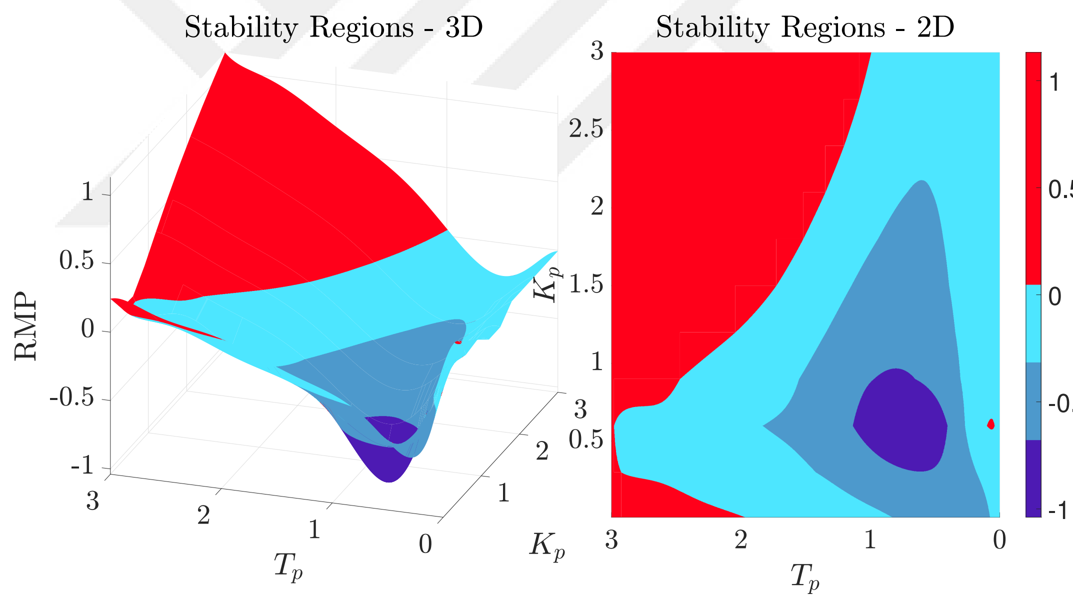

Figure 3.6: Variation of rightmost pole location with respect to simultaneous change in K_p and/or T_p.

3.3.4 Simulation Results

Tracking performances of three different closed loop control systems are presented in Figure 3.7. In the figure, the autonomous flights using a model reference adaptive controller and a closed loop reference model adaptive controller are labeled as MRAC, and CRM, respectively. Human operator controlled flight, where a CRM is used as the controller (See Figure 3.5) is labeled as CRM-H.

This figure, together with Figure 3.8 show that CRM based configurations induce smoother trajectory responses and control inputs. The effect of human operator involvement is also observed as delayed responses to commanded inputs, due to human reaction lag. Overall performance of different configurations, which is defined by the metric

$$\mathcal{M}_e = \mathrm{rms}(e(t))|_{t_a}^{T}, \tag{3.78}$$

where $e(t)$ is the reference model tracking error is provided in Table 3.2. As expected, CRM based controllers provide better tracking performances.

Table 3.2: The tracking performance assessment metric for the MRAC, CRM and CRM-H configurations.

Axes	${\mathcal{M}_e}^{\mathrm{MRAC}}$	${\mathcal{M}_e}^{\mathrm{CRM}}$	${\mathcal{M}_e}^{\mathrm{CRM-H}}$
x	5.153	0.039	0.032
y	11.544	0.041	0.029
z	13.138	3.436	3.435
ψ	0.378	0.001	0.001

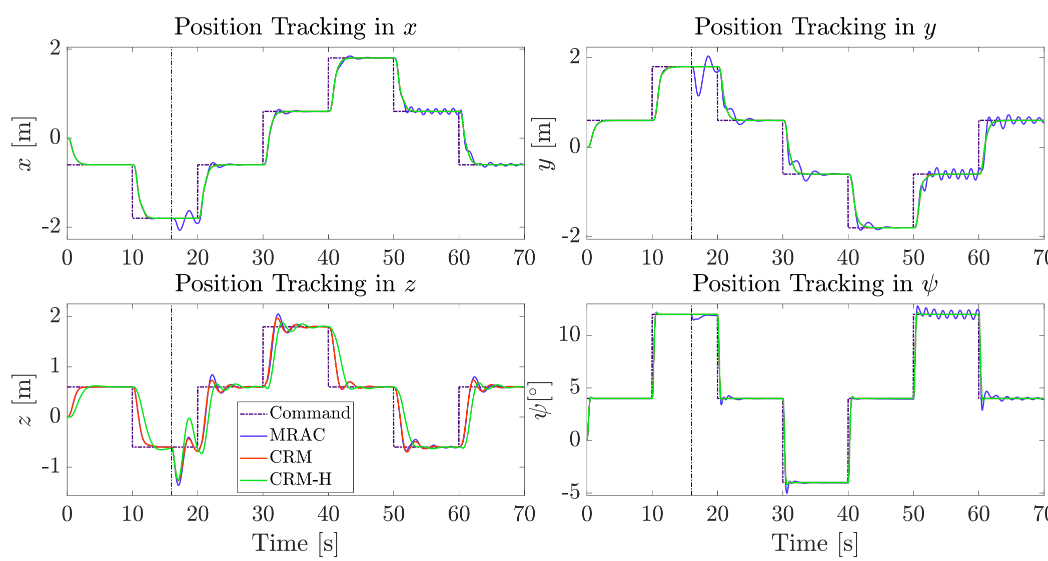

Figure 3.7: The position tracking performance of the MRAC, CRM and CRM-H configurations.

As previously stated in Remark 2, it should be ascertained whether or not control input excitations are close to the natural frequencies of the elastic modes. The natural frequencies, $\bar{\omega}_{kj}$, $k = \{1, 2, 3, 4\}$, $j = \{1, 2, 3\}$, of the first three

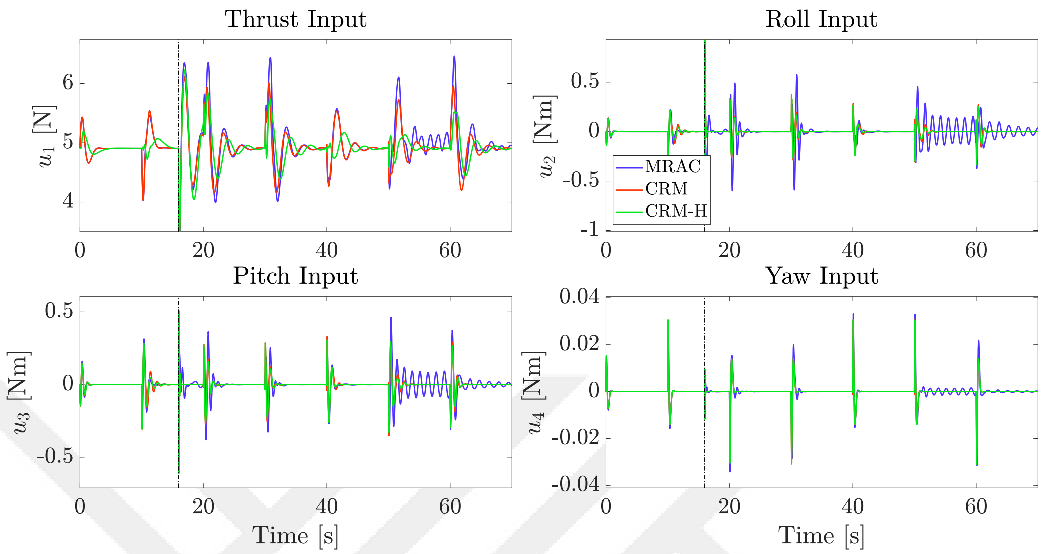

Figure 3.8: The control inputs of the MRAC, CRM and CRM-H configurations.

elastic modes of four quadrotor arms (see (3.43)) are calculated as 131 rad/s, 1365 rad/s and 1865 rad/s, respectively. Figure 3.8 demonstrates that none of the controllers excite these frequencies. On the other hand, it is shown in Figure 3.9 that the arm tip oscillations are lowest in CRM based configurations, which could be predicted from the quadrotor trajectories provided in Figure 3.7.

Variation of the adaptive parameters under the effect of reference changes and anomalies is presented in Figure 3.10. The horizontal dashed black lines in the subfigures denote the projection boundaries. Yellow bands are projection tolerance regions. It is seen that the CRM controllers adapt faster although without any excessive oscillations. They also enter the tolerance region but never exceed the projection boundary.

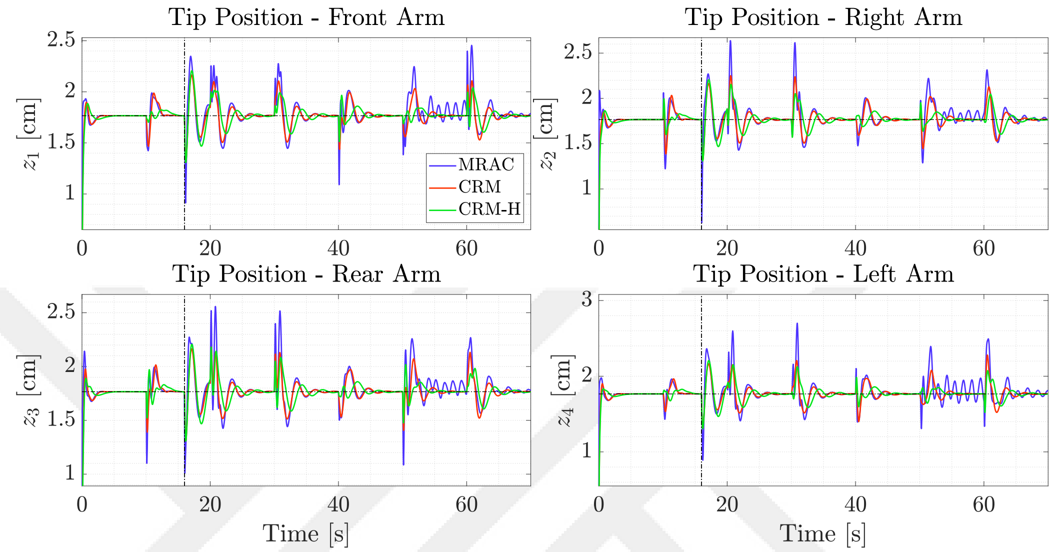

Figure 3.9: The arm tip oscillations of the MRAC, CRM and CRM-H configurations.

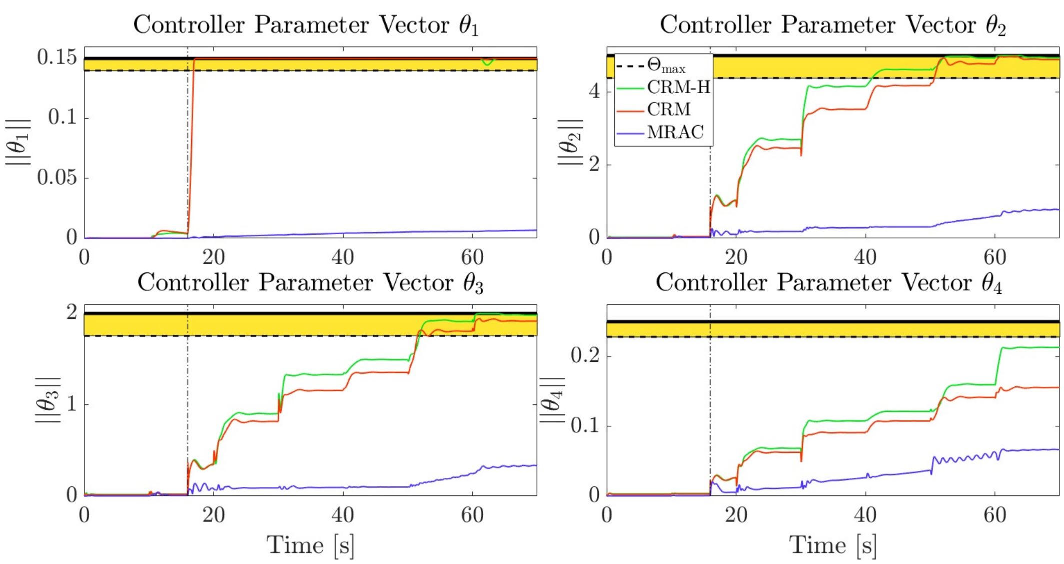

Figure 3.10: The evolution of control parameters of the MRAC, CRM and CRM-H configurations.

Chapter 4

Conclusion and Future Work

As automation becomes more prevalent in engineering systems, creation of new cyber physical & human systems is inevitable. There will be scenarios where humans and machines have to collaborate in combined decision making to have more resilient control systems. These collaborations will require new tools and methodologies. Deeper engagement with the social science community so as to get better insight into human decision making and advanced modeling approaches is necessary. The results reported in this thesis should be viewed as a first of several steps in this research direction. Most of the shared control architectures discussed in the literature do not consider severe anomalies. However, the main aim of the shared control architectures given in this thesis is to provide a bumpless transfer of control between humans and automation, as well as high performance in the presence of severe anomalies. The achievement of this aim is demonstrated using both simulations and experiments.

As future work, further investigations regarding SCA1 and SCA2 can be performed with new experimental sets in order to gain more insight into the mechanism of the anomaly detection. The example of SCA related to flexible UAVs can be verified experimentally and the stability analysis related to the human pilot model can be enhanced with new pilot models.

Bibliography

[1] E. Eraslan, Y. Yildiz, and A. M. Annaswamy, "Shared control between pilots and autopilots: Illustration of a cyber-physical human system," *IEEE Control Systems Magazine*, vol. 40, no. 6, pp. 79–99, 2020.

[2] Y. Yildiz, "Cyberphysical human systems: An introduction to the special issue," *IEEE Control Systems Magazine*, vol. 40, no. 6, pp. 26–28, 2020.

[3] R. A. Hess, "Modeling pilot control behavior with sudden changes in vehicle dynamics," *Journal of Aircraft*, vol. 46, no. 5, pp. 1584–1592, 2009.

[4] R. A. Hess, "A model for pilot control behavior in analyzing potential loss-of-control events," *Proceedings of the Institution of Mechanical Engineers, Part G: Journal of Aerospace Engineering*, vol. 228, no. 10, pp. 1845–1856, 2014.

[5] R. A. Hess, "Modeling human pilot adaptation to flight control anomalies and changing task demands," *Journal of Guidance, Control, and Dynamics*, vol. 39, no. 3, pp. 655–666, 2016.

[6] D. D. Woods and E. Hollnagel, *Joint cognitive systems: Patterns in cognitive systems engineering.* CRC Press, 2006.

[7] D. D. Woods and M. Branlat, "Basic patterns in how adaptive systems fail," *Resilience engineering in practice*, pp. 127–144, 2011.

[8] National Transportation Safety Board, "In-flight icing encounter and loss of control, Simmons Airlines, D.B.A. American Eagle Flight 4184 Avions De

Transport Regional (ATR) model 72-212, N401am Roselawn, Indiana October 31, 1994, NTSB aircraft accident report," NTSB/AAR-96/01, Washington, D.C., 1996.

[9] D. D. Woods, "The theory of graceful extensibility: basic rules that govern adaptive systems," *Environment Systems and Decisions*, vol. 38, no. 4, pp. 433–457, 2018.

[10] D. A. Abbink, T. Carlson, M. Mulder, J. C. de Winter, F. Aminravan, T. L. Gibo, and E. R. Boer, "A topology of shared control systems - finding common ground in diversity," *IEEE Transactions on Human-Machine Systems*, vol. 48, no. 5, pp. 509–525, 2018.

[11] T. B. Sheridan, *Monitoring behavior and supervisory control*, vol. 1. Springer Science & Business Media, 2013.

[12] M. Mulder, D. A. Abbink, and E. R. Boer, "Sharing control with haptics: Seamless driver support from manual to automatic control," *Human factors*, vol. 54, no. 5, pp. 786–798, 2012.

[13] J. Smisek, E. Sunil, M. M. van Paassen, D. A. Abbink, and M. Mulder, "Neuromuscular-system-based tuning of a haptic shared control interface for uav teleoperation," *IEEE Transactions on Human-Machine Systems*, vol. 47, no. 4, pp. 449–461, 2016.

[14] D. W. van der Wiel, M. M. van Paassen, M. Mulder, M. Mulder, and D. A. Abbink, "Driver adaptation to driving speed and road width: Exploring parameters for designing adaptive haptic shared control," in *2015 IEEE International Conference on Systems, Man, and Cybernetics*, pp. 3060–3065, IEEE, 2015.

[15] D. B. Kaber, "Adaptive automation," in *The Oxford Handbook of Cognitive Engineering* (J. D. Lee and A. Kirlik, eds.), Oxford: Oxford University Press, 2013.

[16] K. Ackerman, E. Xargay, D. A. Talleur, R. S. Carbonari, A. Kirlik, N. Hovakimyan, I. M. Gregory, C. M. Belcastro, A. Trujillo, and B. D. Seefeldt,

"Flight envelope information-augmented display for enhanced pilot situational awareness," in *AIAA Infotech@ Aerospace*, p. 1112, 2015.

[17] N. Tekles, F. Holzapfel, E. Xargay, R. Choe, N. Hovakimyan, and I. M. Gregory, "Flight envelope protection for nasa's transport class model," in *AIAA Guidance, Navigation, and Control Conference*, p. 0269, 2014.

[18] J. Chongvisal, N. Tekles, E. Xargay, D. Talleur, A. Kirlik, and N. Hovakimyan, "Loss-of-control prediction and prevention for nasa's transport class model," in *AIAA guidance, navigation, and control conference*, p. 0784, 2014.

[19] E. Eraslan and Y. Yildiz, "Modeling, control and human-in-the-loop stability analysis of an elastic quadrotor," *arXiv preprint arXiv:2012.05747*, 2020.

[20] A. Farjadian, A. Annaswamy, and D. Woods, "A resilient shared control architecture for flight control," in *Proceedings of the International Symposium on Sustainable Systems and Technologies*, 2016.

[21] B. T. Thomsen, A. M. Annaswamy, and E. Lavretsky, "Shared control between adaptive autopilots and human operators for anomaly mitigation," *IFAC-PapersOnLine*, vol. 51, no. 34, pp. 353–358, 2019.

[22] A. B. Farjadian, B. Thomsen, A. M. Annaswamy, and D. D. Woods, "Resilient flight control: An architecture for human supervision of automation," *IEEE Transactions on Control Systems Technology*, 2019.

[23] E. Lavretsky and K. Wise, *Robust and Adaptive Control.* Springer London, 2013, 2013.

[24] K. S. Narendra and A. M. Annaswamy, *Stable adaptive systems.* Courier Corporation, 2005.

[25] S. P. Karason and A. M. Annaswamy, "Adaptive control in the presence of input constraints," in *1993 American Control Conference*, pp. 1370–1374, IEEE, 1993.

[26] E. Lavretsky and N. Hovakimyan, "Stable adaptation in the presence of input constraints," *Systems & control letters*, vol. 56, no. 11-12, pp. 722–729, 2007.

[27] T.-G. Lee and U.-Y. Huh, "An error feedback model based adaptive controller for nonlinear systems," in *ISIE'97 Proceeding of the IEEE International Symposium on Industrial Electronics*, pp. 1095–1100, IEEE, 1997.

[28] T. E. Gibson, A. M. Annaswamy, and E. Lavretsky, "On adaptive control with closed-loop reference models: transients, oscillations, and peaking," *IEEE Access*, vol. 1, pp. 703–717, 2013.

[29] A. E. Bryson, "Optimal control-1950 to 1985," *IEEE Control Systems Magazine*, vol. 16, no. 3, pp. 26–33, 1996.

[30] D. T. McRuer and E. S. Krendel, "Mathematical models of human pilot behavior," tech. rep., Advisory Group for Aerospace Research and Development, 1974.

[31] M. Lone and A. Cooke, "Review of pilot models used in aircraft flight dynamics," *Aerospace Science and Technology*, vol. 34, pp. 55–74, 2014.

[32] S. Xu, W. Tan, A. V. Efremov, L. Sun, and X. Qu, "Review of control models for human pilot behavior," *Annual Reviews in Control*, vol. 44, pp. 274–291, 2017.

[33] D. T. McRuer and H. R. Jex, "A review of quasi-linear pilot models," *IEEE transactions on human factors in electronics*, no. 3, pp. 231–249, 1967.

[34] R. D. Wierenga, "An evaluation of a pilot model based on kalman filtering and optimal control," *IEEE Transactions on Man-Machine Systems*, vol. 10, no. 4, pp. 108–117, 1969.

[35] D. L. Kleinman, S. Baron, and W. Levison, "An optimal control model of human response part i: Theory and validation," *Automatica*, vol. 6, no. 3, pp. 357–369, 1970.

[36] R. Hosman and H. Stassen, "Pilot's perception and control of aircraft motions," *IFAC Proceedings Volumes*, vol. 31, no. 26, pp. 311–316, 1998.

[37] R. A. Hess, "Unified theory for aircraft handling qualities and adverse aircraft-pilot coupling," *Journal of Guidance, Control, and Dynamics*, vol. 20, no. 6, pp. 1141–1148, 1997.

[38] D. D. Woods and N. B. Sarter, "Learning from automation surprises and going sour accidents," *Cognitive engineering in the aviation domain*, pp. 327–353, 2000.

[39] A. B. Farjadian, A. M. Annaswamy, and D. Woods, "Bumpless reengagement using shared control between human pilot and adaptive autopilot," *IFAC-PapersOnLine*, vol. 50, no. 1, pp. 5343–5348, 2017.

[40] S. Tohidi and Y. Yildiz, "Adaptive human pilot model for uncertain systems," in *2019 18th European Control Conference (ECC)*, pp. 2938–2943, IEEE, 2019.

[41] B. L. Stevens, F. L. Lewis, and E. N. Johnson, *Aircraft control and simulation: dynamics, controls design, and autonomous systems*. John Wiley & Sons, 2015.

[42] L. T. Nguyen, M. E. Ogburn, W. P. Gilbert, K. S. Kibler, P. W. Brown, and P. L. Deal, "Simulator study of stall/post-stall characteristics of a fighter airplane with relaxed longitudinal static stability.[f-16]," 1979.

[43] M. R. Waszak and D. K. Schmidt, "Flight dynamics of aeroelastic vehicles," *Journal of Aircraft*, vol. 25, no. 6, pp. 563–571, 1988.

[44] S. S. Rao, *Vibration of continuous systems (Vol. 464)*. New York: Wiley, 2007.

[45] O. A. Bauchau and J. I. Craig, *Structural analysis: with applications to aerospace structures (Vol. 163)*. Science & Business Media: Springer, 2009.

[46] R. Vepa, *Flight Dynamics, Simulation, and Control: For Rigid and Flexible Aircraft*. CRC Press, 2014.

[47] M. R. Waszak, J. B. Davidson, and D. K. Schmidt, "A simulation study of the flight dynamics of elastic aircraft," *Volume*, vol. 1, 1987.

[48] R. F. Stengel, *Flight dynamics*. Princeton University Press, 2015.

[49] N. X. Vinh, *Flight mechanics of high-performance aircraft (Vol. 4)*. Cambridge University Press, 1995.

[50] H. Hesse, R. Palacios, and J. Murua, "Consistent structural linearization in flexible aircraft dynamics with large rigid-body motion," *AIAA journal*, vol. 52, no. 3, pp. 528–538, 2014.

[51] L. V. Schmidt, *Introduction to aircraft flight dynamics.* American Institute of Aeronautics and Astronautics, 1998.

[52] G. Dussart, V. Portapas, A. Pontillo, and M. Lone, *Flight dynamic modelling and simulation of large flexible aircraft.* Techniques and Technologies: Flight Physics-Models, 2018.

[53] S. Bouabdallah, *Design and control of quadrotors with application to autonomous flying (No.* THESIS). Epfl, 2007.

[54] F. Sabatino, *Quadrotor control: modeling.* and simulation: nonlinearcontrol design, 2015.

[55] S. N. Mahmoodi, S. E. Khadem, and M. Kokabi, "Non-linear free vibrations of kelvin–voigt visco-elastic beams," *International Journal of Mechanical Sciences*, vol. 49, no. 6, pp. 722–732, 2007.

[56] M. Romaszko, B. Sapiński, and A. Sioma, "Forced vibrations analysis of a cantilever beam using the vision method," *Journal of Theoretical and Applied Mechanics*, vol. 53, 2015.

[57] M. I. Friswell and A. W. Lees, "The modes of non-homogeneous damped beams," *Journal of Sound and Vibration*, vol. 242, no. 2, pp. 355–361, 2001.

[58] M. Gürgöze and H. Erol, "Dynamic response of a viscously damped cantilever with a viscous end condition," *Journal of Sound and Vibration*, vol. 298, no. 1-2, pp. 132–153, 2006.

[59] Z. T. Dydek, A. M. Annaswamy, and E. Lavretsky, "Adaptive control of quadrotor uavs: A design trade study with flight evaluations," *IEEE Transactions on control systems technology*, vol. 21, no. 4, pp. 1400–1406, 2012.

[60] T. Gibson, A. Annaswamy, and E. Lavretsky, "Improved transient response in adaptive control using projection algorithms and closed loop reference

models," *In AIAA Guidance, Navigation, and Control Conference*, vol. 4775, 2012.

[61] T. T. Tran, S. S. Ge, and W. He, "Adaptive control of a quadrotor aerial vehicle with input constraints and uncertain parameters," *International Journal of Control*, vol. 91, no. 5, pp. 1140–1160, 2018.

[62] S. S. Tohidi, Y. Yildiz, and I. Kolmanovsky, "Adaptive control allocation for constrained systems," *Automatica*, vol. 121, no. 2020, pp. 5–1098, 2020.

[63] S. Islam, P. X. Liu, and A. El Saddik, "Nonlinear robust adaptive sliding mode control design for miniature unmanned multirotor aerial vehicle," *International Journal of Control, Automation and Systems*, vol. 15, no. 4, pp. 1661–1668, 2017.

[64] A. L'Afflitto and T. A. Blackford, "Constrained dynamical systems, robust model reference adaptive control, and unreliable reference signals," *International Journal of Control*, vol. 93, no. 5, pp. 1039–1052, 2020.

[65] A. J. Thurling, "Improving uav handling qualities using time delay compensation," *AFIT/GAB/ENY/00M-0*, vol. 1, 2000.

[66] J. B. Witte, *An investigation relating longitudinal pilot-induced oscillation tendency rating to describing function predictions for rate-limited actuators.* Air Force Institute of Tech Wright-Patterson AFB OH School of Engineering and Management, 2004.

[67] C. . Miller, "Nonlinear dynamic inversion baseline control law: architecture and performance predictions," *In AIAA Guidance, Navigation, and Control Conference*, vol. 6467.

[68] T. Yucelen, Y. Yildiz, R. Sipahi, E. Yousefi, and N. T. Nguyen, "Stability analysis of human-adaptive controller interactions," *In AIAA Guidance, Navigation , and Control Conference*, vol. 1493, 2017.

[69] Z. Dydek, H. Jain, J. Jang, A. Annaswamy, and E. . Lavretsky, "Theoretically verifiable stability margins for an adaptive controller," *In AIAA Guidance, Navigation, and Control Conference and Exhibit*, vol. 6416.

[70] Y. Yildiz, A. M. Annaswamy, D. Yanakiev, and I. Kolmanovsky, “Spark ignition engine fuel-to-air ratio control: An adaptive control approach. control engineering practice,” vol. 18, no. 12, pp. 1369–1378, 2010.

[71] K. Engelborghs, T. Luzyanina, and D. Roose, “Numerical bifurcation analysis of delay differential equations using dde-biftool. acm transactions on mathematical software (toms),” vol. 28, no. 1, pp. 1–21, 2002.

Appendix A

The Normalization Constant

Let

$$\bar{\beta}_j^* = \frac{\cos\bar{\beta}_j + \cosh\bar{\beta}_j}{\sin\bar{\beta}_j + \sinh\bar{\beta}_j} \tag{A.1}$$

Substituting (A.1) into (3.36), we obtain

$$W_j(\bar{x}) = \bar{\gamma}_j\left[(\cos\beta_j\bar{x} - \cosh\beta_j\bar{x}) - \bar{\beta}_j^*\left(\sin\beta_j\bar{x} - \sinh\beta_j\bar{x}\right),\right] \tag{A.2}$$

The normalization constant $\bar{\gamma}_j$ in (A.2) can be calculated by the orthogonality of mode shape $W_j(\bar{x})$ as

$$\int_0^{L_c} \rho_c A_c W_j^2(\bar{x})d\bar{x} = 1, \tag{A.3}$$

$$\int_0^{L_c} \rho_c A_c \bar{\gamma}_j^2[(\cos\beta_j\bar{x} - \cosh\beta_j\bar{x}) - \bar{\beta}_j^*\left(\sin\beta_j\bar{x} - \sinh\beta_j\bar{x}\right)]^2 d\bar{x} = 1. \tag{A.4}$$

Solving (A.4), the normalization constant is obtained as

$$\bar{\gamma}_j = \frac{1}{\sqrt{\rho_c A_c \gamma_c}}, \tag{A.5}$$

where

$$\begin{aligned}\gamma_c = \frac{1}{4\beta}\big[&-\bar{\beta}_j^{*2}\sin(2\bar{\beta}_j) + \bar{\beta}_j^{*2}\sinh(2\bar{\beta}_j) + 4\bar{\beta}_j^{*2}\cos(\bar{\beta}_j)\sinh(\bar{\beta}_j)\\ &- 4(\bar{\beta}_j^{*2}+1)\sin(\bar{\beta}_j)\cosh(\bar{\beta}_j) + 2\bar{\beta}_j^*\cos(2\bar{\beta}_j) - 2\bar{\beta}_j^*\cosh(2\bar{\beta}_j)\\ &+ 8\bar{\beta}_j^*\sin(\bar{\beta}_j)\sinh(\bar{\beta}_j) + 4\bar{\beta}_j + \sin(2\bar{\beta}_j) + \sinh(2\bar{\beta}_j) - 4\cos(\bar{\beta}_j)\sinh(\bar{\beta}_j)\big].\end{aligned} \tag{A.6}$$

Appendix B

The Application of the Orthogonality Conditions

Recall that the partial differential equations of motion for a damped Euler-Bernoulli beam is given as

$$E_c J_c \frac{\partial^4 w(\bar{x},t)}{\partial \bar{x}^4} + \rho_c A_c \frac{\partial^2 w(\bar{x},t)}{\partial t^2} + \sigma_c \frac{\partial w(\bar{x},t)}{\partial t} = F(\bar{x},t). \tag{B.1}$$

Using (3.5) and applying separation of variables, it can be obtained that

$$E_c J_c \frac{d^4 W_j(\bar{x})}{d\bar{x}^4} = \rho_c A_c \bar{\omega}_j^2 W_j(\bar{x}). \tag{B.2}$$

Substituting (B.2) into (B.1) and using (3.5), it follows that

$$\rho_c A_c \bar{\omega}_j^2 W_j(\bar{x}) \Upsilon_j(t) + \rho_c A_c W_j(\bar{x}) \ddot{\Upsilon}_j(t) + \sigma_c W_j(\bar{x}) \dot{\Upsilon}_j(t) = F(\bar{x},t). \tag{B.3}$$

Recall that the orthogonality conditions can be written as

$$\int_0^{L_c} \rho_c A_c W_j(\bar{x}) W_l(\bar{x}) d\bar{x} = \delta_{jl}, \tag{B.4}$$

where δ_{jl} is the Kronecker delta. Multiplying (B.3) by $W_l(\bar{x})$ and integrating it from 0 to L_c, it is obtained that

$$\begin{aligned}
\sum_{j=1}^{\infty} \bar{\omega}_j^2 \Upsilon_j(t) \int_0^{L_c} \rho_c A_c W_j(\bar{x}) W_l(\bar{x}) d\bar{x} + \\
\sum_{j=1}^{\infty} \ddot{\Upsilon}_j(t) \int_0^{L_c} \rho_c A_c W_j(\bar{x}) W_l(\bar{x}) d\bar{x} + \\
\frac{\sigma_c}{\rho_c A_c} \sum_{j=1}^{\infty} \dot{\Upsilon}_j(t) \int_0^{L_c} \rho_c A_c W_j(\bar{x}) W_l(\bar{x}) d\bar{x} = \int_0^{L_c} W_l(\bar{x}) F(\bar{x}, t) d\bar{x}.
\end{aligned} \tag{B.5}$$

In view of the orthogonality conditions given by (B.4), it is obtained that

$$\ddot{\Upsilon}_j(t) + \sigma_c' \dot{\Upsilon}_j(t) + \bar{\omega}_j^2 \Upsilon_j(t) = \int_0^{L_c} W_j(\bar{x}) F(\bar{x}, t) d\bar{x}, \tag{B.6}$$

where $\sigma_c' = \sigma_c/(\rho_c A_c)$ is a constant.